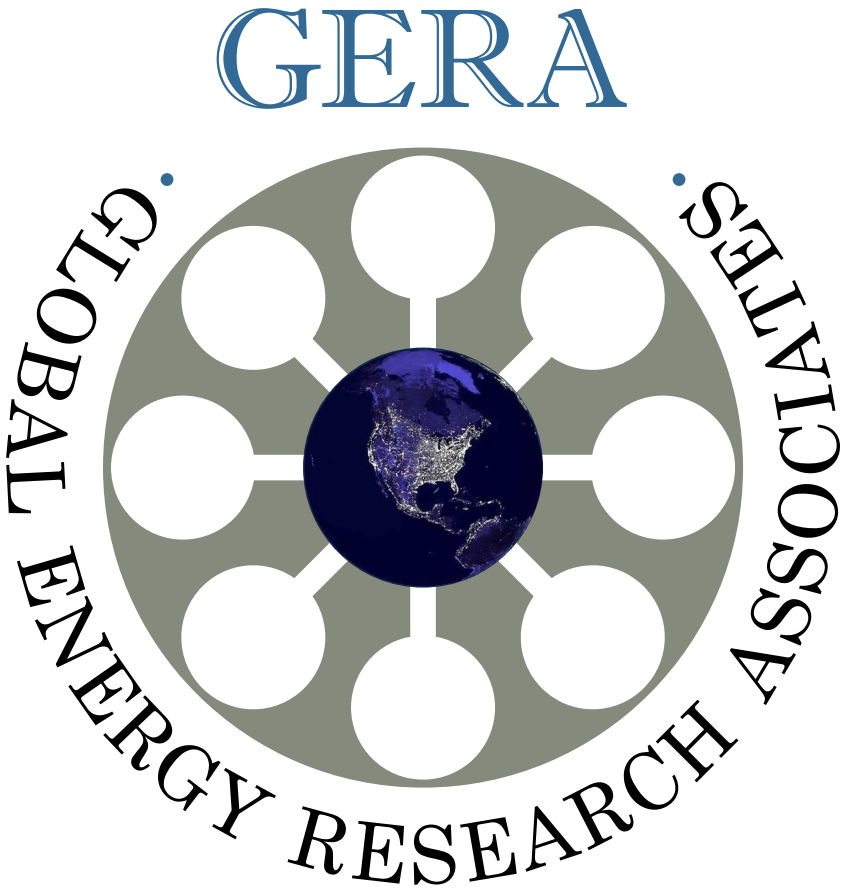
Nanofuel internal engine

Mark L. Adams, Ph.D.*

September 3, 2015

GERA-2015-01



Global Energy Research Associates (GERA)

340 Broadway, Saratoga Springs, New York 12866

Providing energy solutions

*email: adams@gera.co | phone: +1-518-871-1173 | fax: +1-518-871-1286

Disclaimer

This report is a preprint of a paper intended for publication in a journal or proceedings and includes information that is the sole property of Global Energy Research Associates LLC. All Rights Reserved.

Auspices

This work was funded through an independent research and development (IRAD) project under the auspices of Global Energy Research Associates LLC.

Nanofuel internal engine

Mark L. Adams, Ph.D.

September 3, 2015

Abstract

This paper presents an inventive nanofuel internal engine, whereby nuclear energy is released in the working fluid and directly converted into useful work, with the qualities of an economical advanced small modular gaseous pulsed thermal reactor.

Scientific feasibility is established by studying the behavior of nuclear fuels in configurations designed to support a fission chain reaction. Nanofuel is defined as nuclear fuel suitable for use in an internal engine, comprised of six essential ingredients, and can be created from clean fuel or from the transuranic elements found in light-water reactor spent nuclear fuel in a proliferation resistant manner. Three essential ingredients ensure the nanofuel is inherently stable, due to a negative temperature coefficient of reactivity. Reciprocating and Wankel (rotary) internal engine configurations, which operate in an Otto cycle, are adapted to support a fission chain reaction. Dynamic engine cores experience a decrease in criticality as the engine piston or rotor moves away from the top dead center position. In this inherent safety feature, the increase in engine core volume decreases the nanofuel density and increases the neutron leakage.

Technological feasibility is demonstrated by examining potential engineering limitations. The nanofuel internal engine can be operated in two modes: spark-ignition with an external neutron source such as a fusion neutron generator; and compression-ignition with an internal neutron source. The structural integrity can be maintained using standard internal-combustion engine design and operation practices. The fuel system can be operated in a closed thermodynamic cycle, which allows for complete fuel utilization, continuous refueling, and easy fission product extraction.

Nanofuel engine power plant configurations offer favorable economic, safety, and waste management attributes when compared to existing power generation technology. The initial (first-of-a-kind) overnight capital cost is approximately $400 per kilowatt-electric. Obvious safety features include an underground installation, autonomous operation, and an ultra-low nuclear material inventory.

1 Introduction

This paper presents an inventive nanofuel internal engine, whereby nuclear energy is released in the working fluid and directly converted into useful work, that has favorable economics, safety, and waste management attributes when compared to existing power generation technology.

During the Industrial Revolution new devices that converted chemical energy into economically useful work begat new manufacturing processes. Launching the Industrial Revolution, Antoine-Laurent Lavoisier, the recognized father of modern chemistry, put forth the theory of combustion and other scientific advances that are vital to the general understanding of chemical energy. In concert, the firm of Boulton & Watt, founded by industrialist Matthew Boulton and engineer James Watt in 1775, successfully commercialized their Watt engine and completely reshaped the energy industry.

Lavoisier's work was a paradigm shifting scientific achievement at the end of the eighteenth century. As described by Thomas S. Kuhn in *The structure of scientific revolutions*, it redefined the legitimate problems and research methods for succeeding generations of practitioners. [1] In a similar fashion, one goal of this paper is to create a local paradigm shift in the energy industry by formulating the scientific basis of a nuclear powered internal engine.

According to Kuhn [1], a necessary condition for a new paradigm is that the work must be:

1. *sufficiently unprecedented to attract an enduring group of adherents away from competing modes of scientific activity;* and
2. *sufficiently open-ended to leave all sorts of problems for the redefined group of practitioners to solve.*

In an effort to attract adherents, this paper culminates with the presentation of a Wankel engine that is powered by nuclear waste or, more specifically, the transuranic elements from existing commercial light-water reactor (LWR) spent nuclear fuel (SNF). Leaving all sorts of problems for future practitioners, this paper uses proven research methods in nuclear engineering to establish a solid technological foundation for the nanofuel internal engine and frame legitimate problems for future exploration.

Boulton & Watt's steam engine produced economically useful work and disrupted the energy industry at the end of the eighteenth century. First, the Watt engine introduced a 75% increase in fuel efficiency over the incumbent Newcomen steam engine. In a bold business move, instead of licensing their engines, Boulton & Watt offered customers a royalty arrangement that amounted to one-third of the fuel savings. The initial Watt engine offered miners

the ability to pump water at half the pervious fuel cost with no capital expenditure for new equipment. Second, through a series of engineering improvements the Watt engine operated as a reliable rotative engine for the rapidly growing textile industry. This innovation displaced the water wheel as the main source of industrial power, reduced the geographical constraints for factories, and ultimately catapulted Europe out of the Dark Ages. [2]

The Watt engine was a commercial success because it had a significant economical advantage over existing engine options. In a similar fashion, another goal of this paper is to establish the nanofuel internal engine as a device capable of converting nuclear energy into economically useful work. Analogous to the Watt engine at the end of the eighteenth century, this energy innovation can disrupt the entire energy industry at the beginning of the twenty-first century and improve the quality of life for present and future generations around the world.

In normal pedagogical fashion, the remainder of this introduction presents a view on the current economic status of commercial nuclear power plant deployment, reviews the history of nuclear powered internal engines, and outlines the sections that follow.

1.1 Economics

Alvin M. Weinberg defined the **first nuclear era** as the time period covering the initial growth of nuclear technology. [3, 4] The first nuclear era lasted over 50 years, witnessed the construction of approximately 500 commercial nuclear reactors worldwide, and ended in 1978 (antecedent to the 1979 Three Mile Island accident) with the last nuclear reactor orders in the United States.

Several elements contributed to the end of this era. Foremost, the commercial nuclear power plant overnight capital cost [5] and construction time steadily increased due to both the **economies of scale** approach to reactor design and the escalating safety requirements imposed by regulatory agencies. Illustrating this point, in 1957 the 60 megawatt-electric (MW_e) Generation I Shippingport Atomic Power Station had an all-in capital cost [6] of 1,200 2012\$/kW_e (2012 US dollars per kilowatt-electric) and a construction time of 32 months [7], while large or gigawatt-electric-scale (GW_e-scale) Generation II nuclear power plants had an all-in capital cost of 2,000-13,000 2004\$/kW_e (2004 US dollars per kilowatt-electric) and an average construction time of 9 years [8].

Further impeding nuclear power evolution during the first nuclear era, Title 10 Code of Federal Regulations Part 50 (10 CFR 50) [9] exposes electric utility companies to the economic risk of having a fully functional nuclear power plant without a license to sell electricity. 10 CFR 50 is a two-step licensing process where the applicant obtains a construction permit

and then an operation licenses. Taken together, these elements created an unacceptably high economic risk for commercial nuclear power plant deployment and brought an end to the first nuclear era.

Today, the world faces an energy crisis that stems from the confluence of unfavorable developments in the areas of energy supply and demand, climate change, and energy security. Let us discuss these areas in greater detail:

Energy supply and demand The US Energy Information Administration predicts a 56% increase in the global energy demand and a steady 80% dependence on fossil fuels (liquids, coal, and natural gas) for the global energy supply from 2010 to 2040. [10]

A majority of the projected growth in energy demand is expected to occur in countries outside the Organization for Economic Cooperation and Development (OECD) [11], known as non-OECD countries. More specifically, over the next 30 years the forecasted growth in energy consumption is 3% per year in non-OECD countries and 0.5% per year in OECD countries. [10] Energy consumption is proportional to the standard of living. Countries with large populations and low gross domestic product (GDP) per capita, such as China and India, are increasing their energy consumption and increasing their economic output.

A majority of the projected growth in energy supply is expected to be from fossil fuels. The forecasted growth in clean energy (renewables and nuclear) consumption through 2040 is disappointingly low.

The price of fossil fuel is volatile and the cost of a fossil fuel power plant doubles when environmentally responsible components, such as carbon capture and sequestration technology, are included. These factors contribute to an increasing economic uncertainty in the global energy industry.

Climate change Fossil fuel combustion is responsible for introducing an unprecedented amount of greenhouse gases into the atmosphere. In particular, carbon dioxide (CO_2) atmospheric concentrations have risen dramatically over the last century. Before the Industrial Revolution, the CO_2 atmospheric concentration was around 280 parts per million (ppm). [12] In 2012, the average CO_2 atmospheric concentration was around 394 ppm. [12] Between 2010 and 2040 the global energy-related annual CO_2 emissions are predicted to increase by 46%, rising from 31.2 billion metric tons in 2010 to 45.5 billion metric tons in 2040. [10]

The impact of greenhouse gas emissions on the climate is an ever-evolving topic. It is known that fluctuations in the CO_2 atmospheric concentration are directly correlated

to the Earth's average temperature. [13] Thus, a high CO_2 atmospheric concentration corresponds to a high average temperature. It is also known that the terrestrial climate is a complex nonlinear system that humans are not able to control. Unfortunately, the most likely outcome of tampering with this system is a critical transition or tipping-point or state shift in the Earth's biosphere. [14] The consequence of such a change would be devastating.

Energy security Energy security encompasses the relationship between an individual nation's energy demands and their ability to mitigate energy supply disruptions. [15] Energy independence describes the concept that an individual nation's energy supply completely meets its energy demand. However, after accounting for foreign policy, every country participates in the global energy market and is not energy independent. Competition over energy resources can rapidly escalate into international conflict.

Consequently, there is an immediate need for sustainable alternative energy sources and, as predicted by Weinberg, a renewed interest in nuclear power.

Nuclear energy is a clean (with respect to greenhouse gas emissions), safe, and sustainable energy source. Commercial nuclear power plants stand alone as the only proven carbon-free large-capacity means of generating electricity. Nuclear fuel has approximately 10^6 times the energy density of fossil fuels. For example, the plutonium isotope 239 (^{239}Pu) contains 80,120,000 kilojoules per gram (kJ/g) [16] and gasoline (C_8H_{17}) contains only 45.92 kJ/g [17]. Even with theses advantages over fossil fuels, the start of the **second nuclear era** (or nuclear renaissance) is struggling for the same reason the first nuclear era ended — economics.

In 1989, the US Nuclear Regulatory Commission (NRC), which succeeded the US Atomic Energy Commission as the federal agency that regulates the peaceful and commercial uses of nuclear material in 1975, introduced several new commercial nuclear power plant licensing options. As set forth in 10 CFR 52 [18], a combined (construction and operation) license (COL) permits both the construction and operation of a new commercial nuclear power plant. The major components of a COL can reference an early site permit (ESP), which covers site or location specific elements, and a design certification (DC), which covers nuclear power reactor design details. [19] From the perspective of an electric utility company, these new licensing options reduce the economic risk of deploying a new nuclear power generating station. However, while this licensing update is an improvement for the deployment of present nuclear technology the capital cost of such an endeavor is still too large.

According to a recent Energy Policy Institute at Chicago (EPIC) report [20], the overnight capital cost of a new GW_e-scale Generation III+ nuclear power plant is 3,617-5,339 2010\$/kW_e. This implies that the overnight capital cost of building a new Westinghouse Electric AP1000

is approximately 3.979-5.873 billion 2010$. The resulting economic risk of such an endeavor is unacceptably high. For example, Moody's Investors Service classified the risk at the *bet-the-farm* level. [21]

Let us turn to an incentive based discussion and ask the question, *Is there a more economical path forward for nuclear power?* Performing a simple commercial nuclear power plant gedanken economic analysis, where the dominant terms are the assets long-term value and all-in capital cost, can shed light on this important economical question. The long-term value is derived from the low cost of nuclear fuel; the all-in capital cost is directly proportional to the plant size and construction time. Given only these terms, it is economically favorable to maintain the low cost of nuclear fuel and reduce either the plant size or construction time. Hence, moving toward smaller capacities (lower overnight capital cost) and shorter construction times (lower financing cost) reduces the economic risk of deploying a nuclear power plant. This is part of the motivation for deploying small modular reactor (SMR) [22, 23] nuclear power plants, and has driven several nuclear reactor vendors around the world to aggressively shift their reactor design philosophy from economies of scale to **economies of mass manufacturing**.

SMRs are characterized by capacities less that 300 MW_e and construction times less than two years, or roughly 18 months for site assembly followed by six months for inspections, tests, analysis, and acceptance criteria (ITAAC). The idealized approach to deploying SMR nuclear power plants starts with the fabrication (and inspection) of SMR components in a controlled factory environment (by highly skilled workers) and is followed by an express site-specific plant assembly. The economic benefits of factory fabrication for complex engineering jobs have been demonstrated in the shipbuilding and aerospace industries, such as manufacturing Space Shuttles. Chiefly, **learning** theory dictates that the unit cost decreases by a constant percentage (the improvement) each time the number of production units doubles. [24] In business management the experience curve expresses a similar concept.

Another economic advantage of deploying a large capacity electricity generation station comprised of several SMR nuclear power plants is that operating plants provide revenue through the sale of electricity and act as a valuable asset in financing additional plants. This reduces the bet-the-farm level of economic risk.

Further motivation for deploying SMRs is found on the safety front. SMRs build on the general safety standards of GW_e-scale Generation III+ nuclear power plants and possess additional safety benefits due to straightforward changes in their design and operation. SMR designs have enhanced passive safety features (eliminating external water and auxiliary power requirements in the event of an accident) and reduced nuclear fuel inventories. Their operation revolves around standardized components (such as common instrumentation and

controls) that improve the operations and maintenance personnel training quality and depth of talent. These increased safety factors decrease the potential risk to the environment and the public in an emergency, increase site location possibilities, and create new markets for nuclear power.

While the economies of mass manufacturing approach to nuclear power plant development are appealing, the desirable economic realization of this approach remains to be seen. A recent EPIC report on the economics of SMRs anticipates the all-in capital cost for the first electricity generation station comprised of six 100 MW_e SMRs is 6,700-11,000 2011\$/kW_e. [25] Although this is economically favorable when compared to other clean alternative energy technology (wind, solar, and biomass), it is unprofitable in the present market. Although the SMR approach to building a nuclear power plant reduces the economic risk of the endeavor by requiring less capital outlay, the larger all-in capital cost per kW_e makes the project less profitable and requires a much longer payback period.

Successful adoption of new nuclear power generation technology will require addressing the present economic challenges hindering the deployment of existing nuclear options. It behooves the energy industry to leverage the enormous nuclear energy density advantage over fossil fuels; it is wise to explore options that fit within existing regulatory requirements; and it is a good idea to leverage the economic and safety advantages of small nuclear technology (minimizing component number and fuel inventory) and modular manufacturing techniques (learning and improving product quality). This paper follows these guidelines and encourages future research in this direction.

1.2 History

Hitherto the idea of a nuclear powered internal engine has been given little consideration. Following World War II, nuclear engine research and development focused on extraterrestrial propulsion applications. [26] In these rocket propulsion systems a working fluid is heated by a nuclear reactor with solid fuel and then expelled through an exhaust nozzle to generate thrust. These propulsion systems are external engines operating in an open thermodynamic cycle, where mass is allowed to cross the system boundary. In sharp contrast, this paper focuses on internal engines operating in a closed thermodynamic cycle.

In 1953 Edward H. Kerner published the first paper on *the possible use of gaseous fissionable materials in an engine of internal-combustion type*. [27] This brief theoretical paper mentions that such an engine could have a relatively small size, a high thermal efficiency, and eliminate the formidable heat-transfer problems in conventional reactors.

In 1967 Richard L. Moore patented what he called a *pulsating nuclear reactor motor*. [28] In this external engine a nuclear reactor with solid fuel heats the working fluid, the working fluid volume increases, and the working fluid performs work on a piston. The nuclear reactor had a negative void coefficient of reactivity to control the release of nuclear energy per cycle. In 1979 Joseph Pettibone conceived of a large water piston external engine driven by a nuclear weapon-like release of nuclear energy. [29, 30] Although this engine had obvious proliferation problems, it highlights the scientific feasibility and the economic advantages of eliminating the nuclear steam supply system.

Previous internal engine designs include the development of a *nuclear piston engine* or *Otto-motor* around 1970. [31, 32] These engines had a reciprocating piston geometry. The housing acted as a moderator and reflector, the engine was fueled with a mixture of uranium isotope 235 hexafluoride ($^{235}UF_6$) and helium, and the device was initiated by an external neutron source. Since this engine was not inherently safe, a second piston and control rods were added to control criticality. In 1991 John Heidrich *et al.* [33–35] designed a reciprocating piston internal engine *featuring a self-shutoff mechanism to provide nuclear safety*. This design emphasized a potential 10-fold reduction in the capital cost of a nuclear power plant and gave considerable attention to the closed fuel cycle. Neither theoretical design was ever reduced to practice.

1.3 Outline

The remainder of this paper is structured as follows:

Section 2: Power cycles reviews the ideal Otto cycle, which provides a simplified thermodynamic description of the pertinent processes in an actual internal engine and enables analytic quantitative comparisons of engine design alternatives, and presents several internal engine power plant configurations

Section 3: Nanofuel explores nuclear fuel compositions that are suitable for use in an internal engine and presents an important inherent safety feature that is characteristic of certain nanofuels, namely the nanofuel negative temperature coefficient of reactivity.

Section 4: Engine core criticality performs theoretical one-speed diffusion theory criticality calculations to estimate the critical size of an engine (reactor) core in a reciprocating nanofuel internal engine and discusses a second inherent safety feature where the dynamic engine core geometry experiences a decrease in criticality as the engine piston moves away from the top dead center crank position.

Section 5: Ideal engine performance returns to the ideal Otto cycle and models nanofuel engine performance.

Section 6: Engine performance models the performance of a generic 4-stroke reciprocating nanofuel engine operating in spark-ignition and compression-ignition mode.

Section 7: LWR SNF nanofuel explores nanofuels comprised of the transuranic elements from LWR SNF and their performance in a nanofuel engine.

Section 8: Wankel nanofuel engine reviews the Wankel engine geometry, adapts the Wankel engine to support a nuclear chain reaction, and explores compact and economical Wankel nanofuel engine configurations.

Section 9: Advanced reactor performance models a Wankel nanofuel engine with a nanofuel comprised of the transuranic elements from LWR SNF.

Section 10: Outlook analyzes the economic, safety, waste management, and nonproliferation attributes of a Wankel nanofuel internal engine electric power plant.

Appendix A: Housing neutron transport analytically determines the probability that a fission neutron is thermalized in the reflector and returned to the engine core.

Appendix B: Housing strength calculates the reciprocating nanofuel engine piston case (housing) deformation due to an internal gaseous nanofuel pressure using the theory of elasticity.

2 Power cycles

Power cycles are thermodynamic cycles that produce useful work. Systems that perform power cycles are commonly called engines and categorized as either external engines or internal engines depending on whether the working fluid is heated by an external source or releases energy, respectively.

Present commercial nuclear power plants, and alternative advanced nuclear power plant concepts, are external engines. Figure 1 illustrates a simplified two-loop Rankine cycle for a pressured water reactor (PWR) nuclear power plant. [36] In this external engine there are several stages between the release of nuclear energy in the reactor and the production of useful work by the turbine. At a minimum:

1. the solid fuel in the reactor releases nuclear energy;
2. the primary coolant extracts heat from the solid fuel in the reactor;

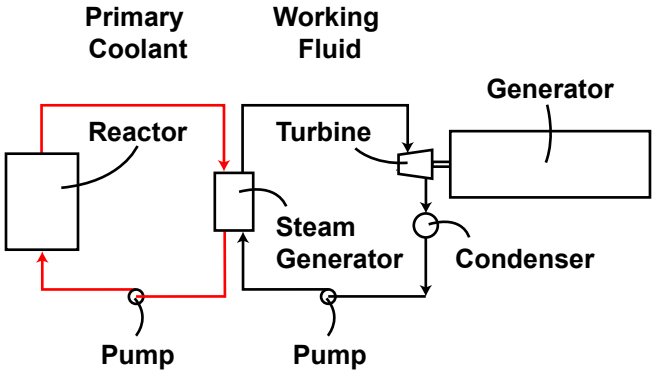


Figure 1: **Simplified two-loop Rankine cycle for a pressured water reactor (PWR) nuclear power plant.**

3. the working fluid extracts heat from the primary coolant in the steam generator; and
4. the turbine extracts heat from the working fluid and produces work in the form of a rotating shaft that drives the electric generator.

Every stage incurs a cost.

Internal engines are the most reliable and widely used power source in the world. This paper builds on the mature science of designing and operating internal engines that release chemical energy and introduces the design and operation of high-power internal engines that release nuclear energy.

This section reviews the ideal Otto cycle, which provides a simplified thermodynamic description of the pertinent processes in an actual internal engine and enables analytic quantitative comparisons of engine design alternatives. This section also presents several internal engine power plant configurations.

2.1 Otto cycle

The reciprocating internal engine is a convenient device for reviewing the ideal Otto cycle. In this device a piston oscillates in a cylinder and transmits power to a rotating shaft. Figure 2 illustrates the two main piston stopping positions in a reciprocating internal engine, namely the bottom dead center (BDC) crank position and the top dead center (TDC) crank position. Figure 3 illustrates the ideal Otto cycle process diagram.

The ideal Otto cycle assumes that all processes are internally reversible and the working fluid is an ideal gas with constant specific heats. The cycle begins in state 1, where the

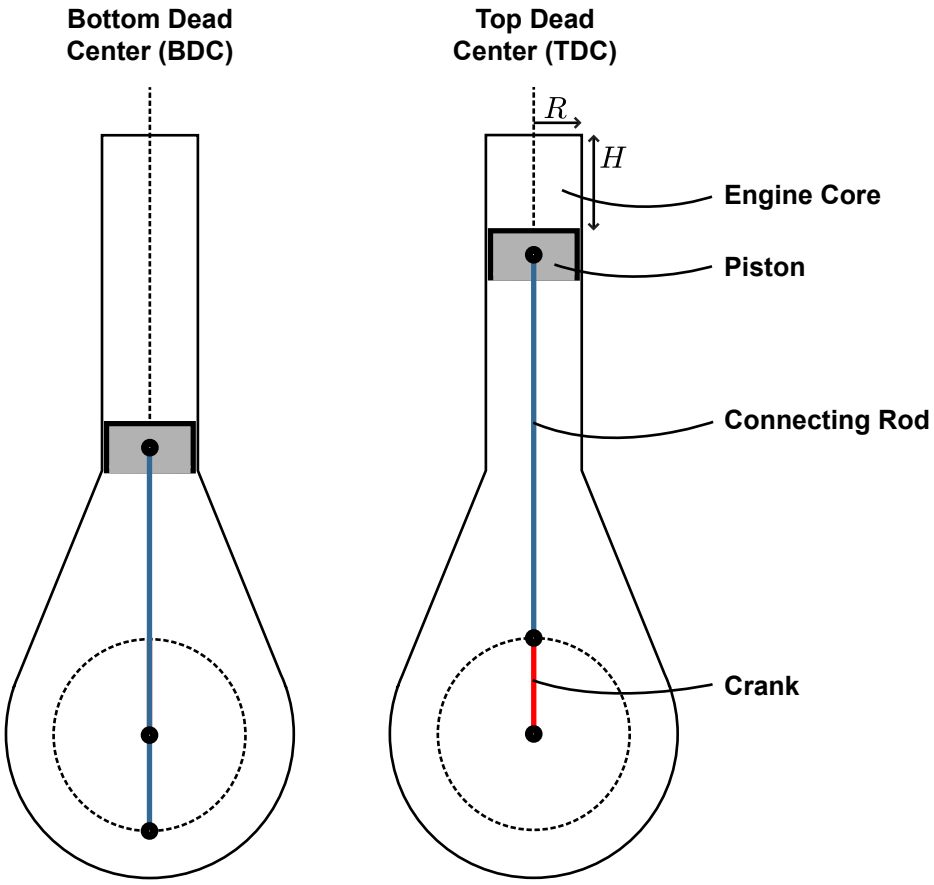


Figure 2: **Reciprocating internal engine piston stopping positions, namely the bottom dead center (BDC) crank position (left) and the top dead center (TDC) crank position (right).**

piston is located in the BDC crank position. A mass of fuel (M), which is also the working fluid, is confined within a cylinder (or engine core) of volume $V_1 = \pi R^2 H_1$, where R (H) is the cylinder radius (height) and the subscripts refer to the cycle state.

The ideal Otto cycle processes and their common internal-combustion engine labels are:

Compression During process 1-2 the working fluid is isentropically compressed and in state 2 the piston is located in the TDC crank position (see Fig. 2).

Combustion During process 2-3 the working fluid internal energy (U) increases at constant volume.

Expansion During process 3-4 the working fluid isentropically expands and in state 4 the piston returns to the BDC crank position (see Fig. 2).

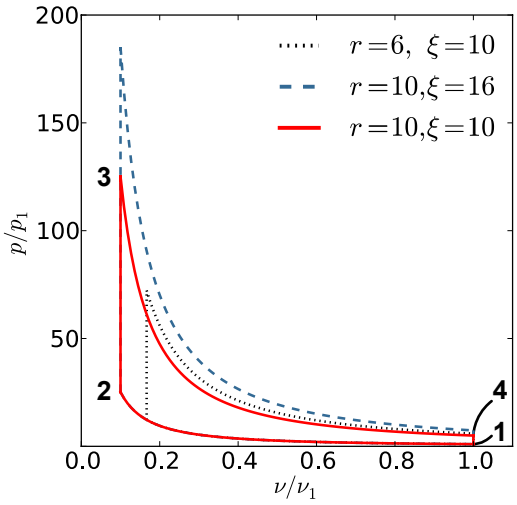


Figure 3: **Ideal Otto cycle process diagram illustrating variations in the dimensionless parameters r and ξ: solid (red) curve, $r = 10$ and $\xi = 10$; dashed (blue) curve, $r = 10$ and $\xi = 16$; and dotted (black) curve, $r = 6$ and $\xi = 10$.**

Exhaust and Intake During process 4-1 the working fluid exits the engine and returns to the engine through an engine specific exhaust and intake process.

In actual internal engines there is a certain degree of irreversibility. [37]

Two dimensionless parameters describe the ideal Otto cycle. First, the compression ratio is given by

$$r = \frac{\nu_1}{\nu_2} = \frac{\rho_2}{\rho_1} = \frac{H_1}{H_2}, \tag{1}$$

where $\nu = V/M$ ($\rho = M/V$) is the working fluid specific volume (mass density). Second, the ratio of the energy deposited in the working fluid during process 2-3 (Q) to the working fluid internal energy in state 1 (U_1) defines the following parameter (ξ):

$$\xi = \frac{Q}{U_1}. \tag{2}$$

With these dimensionless quantities, several ideal Otto cycle thermodynamic properties can be conveniently expressed relative to their initial state.

Another important dimensionless parameter is the thermal efficiency (η). The ideal Otto cycle thermal efficiency for a working fluid with constant specific heat ratio (γ) is given by

$$\eta = 1 - r^{1-\gamma}. \tag{3}$$

For $\gamma > 1$, this formula shows that η increases with r.

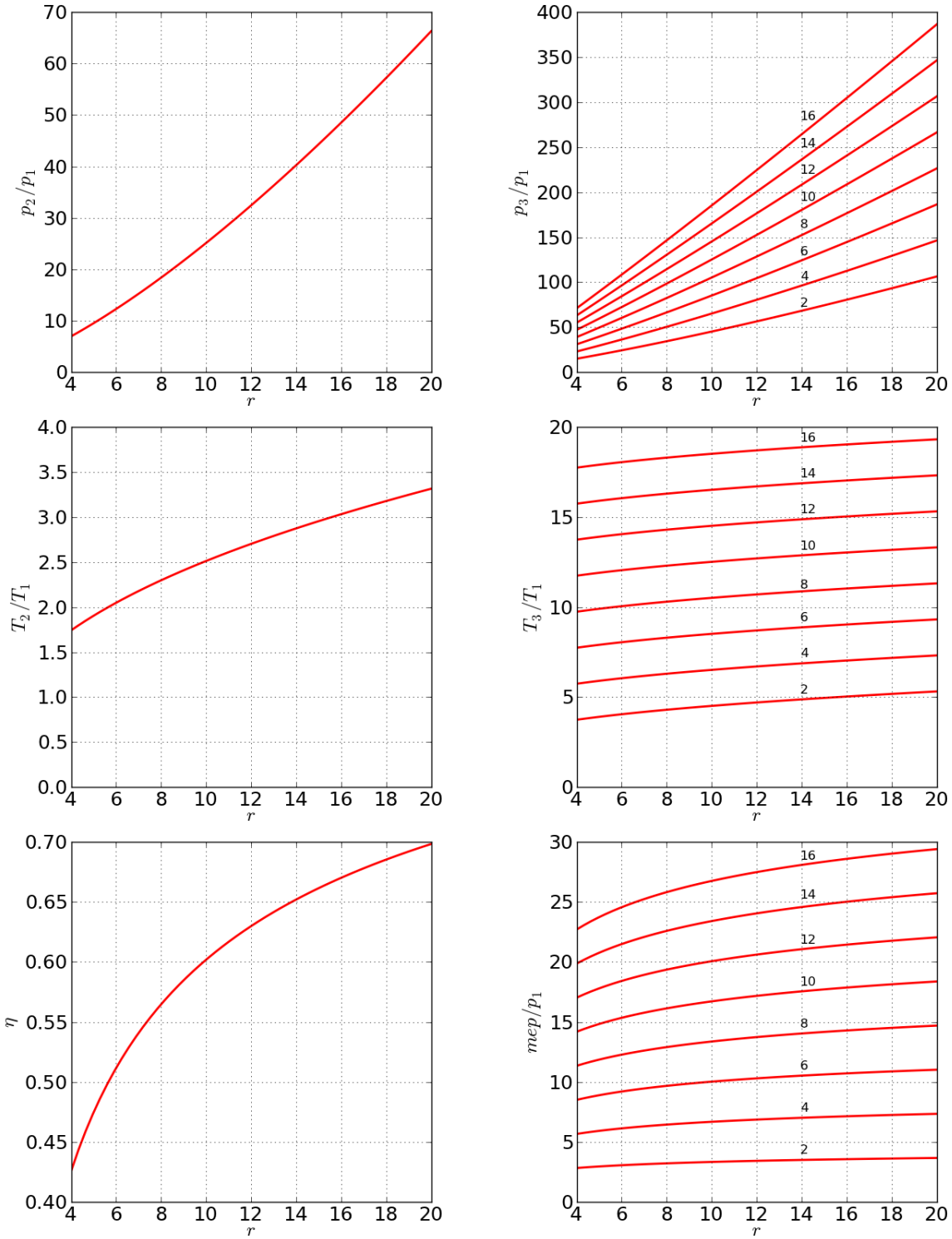


Figure 4: **Characteristics of the ideal Otto cycle as a function of the dimensionless parameters r and ξ. Curve labels correspond to ξ.**

Similar to the dimensionless representation of the air cycle given by Taylor [17], the working fluid pressure (p) and temperature (T) at several states can be written as:

$$\frac{p_2}{p_1} = r^{\gamma}, \qquad \frac{p_3}{p_1} = r^{\gamma} + r\xi, \tag{4}$$

$$\frac{T_2}{T_1} = r^{\gamma-1}, \qquad \frac{T_3}{T_1} = r^{\gamma-1} + \xi. \tag{5}$$

It is also useful to define the mean effective pressure (mep) as the ratio of the net work done by the cycle to the cylinder displacement volume, which is the difference between the maximum (BDC) and minimum (TDC) cylinder volumes. In terms of dimensionless parameters the mep is given by

$$\frac{\text{mep}}{p_1} = \xi \frac{1 - \left(\frac{1}{r}\right)^{\gamma-1}}{(\gamma - 1)\left(1 - \frac{1}{r}\right)}. \tag{6}$$

The work done in applying the mep to the piston during the expansion stroke is equivalent to the work of the actual cycle. Figure 4 illustrates these expressions.

2.2 Power plant configurations

The internal engine directly couples to a rotating shaft that can drive an electric generator. In an internal engine, the expansion stroke (or process 3-4) directly converts the energy absorbed in the working fluid during the combustion process (or process 2-3) into useful work in the form of a rotating shaft that can drive an electric generator. This direct coupling significantly reduces the number of components in a power plant and dramatically reduces cost.

For internal engines that release nuclear energy, several simple power plant configurations provide environmental benefits and increase the power cycle economics. A closed recycling fuel system isolates the working fluid in the power plant from the surrounding environment and improves fuel utilization. A supercharging system or turbine increases the engine power and efficiency. Supercharging systems use compressors or pumps or blowers to increase the inlet working fluid density (ρ_1). Turbines produce additional useful work by extracting energy from the exhaust.

Figure 5 illustrates a turbocharged engine. The red loop represents a closed recycling fuel system that is suitable for nuclear material. This configuration uses a compressor to increase the inlet working fluid density and a turbine to extract energy from the exhaust. The turbocharger compressor and turbocharger turbine are connected on a single shaft.

Figure 6 illustrates an alternative engine configuration that involves mechanical supercharging and turbocompounding. [37] Mechanical supercharging uses a compressor powered by

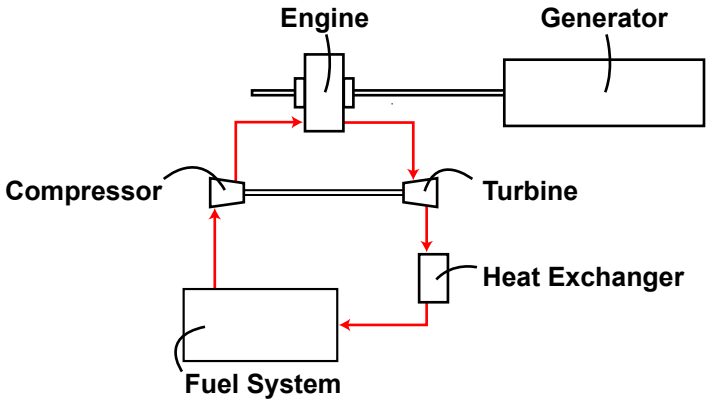


Figure 5: **In a turbocharged engine the turbocharger compressor and turbocharger turbine are connected on a single shaft.**

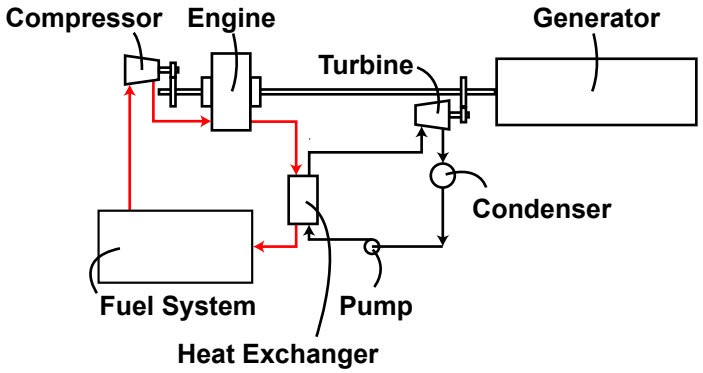


Figure 6: **Power plant configuration involving mechanical supercharging (compressor) and turbocompounding (turbine).**

the drive shaft to increase the inlet working fluid density. Turbocompounding uses a turbine connected to the drive shaft to increase the overall system power and efficiency. This configuration simplifies the system components in contact with nuclear material.

3 Nanofuel

Nuclear engineering is a mature science with proven research methods. Divide and conquer is the traditional approach to begin studying the behavior of a nuclear fuel in a configuration designed to support a fission chain reaction. For example, the effective multiplication factor (k_{eff}), which describes the possible fate of neutrons in a finite system for a given fission generation, is calculated by division into an infinite medium multiplication factor (k_{∞}), which depends on the nuclear fuel, and a nonleakage probability (P_{NL}), which depends on the reactor core geometry. [16, 38–40]

This section explores nuclear fuel compositions that are suitable for use in an internal engine. These fuels are called **nanofuels**, where the prefix *nano* is added to emphasize the general presence of molecules and complex clusters that have dimensions on the nanometer scale and introduce quantum statistical phenomena that affect engine performance. The prefix is also a tribute to Richard P. Feynman's famous paper, *There's plenty of room at the bottom.* [41]

Nanofuel is comprised of six general ingredients:

Fissile Fuel Nuclides that undergo thermal neutron induced fission. Common examples include: ^{233}U, ^{235}U, and ^{239}Pu.

Passive Agent Nuclides that have a resonance neutron absorption cross-section in the low epithermal energy range. Common examples with a strong resonance neutron absorption cross-section near 1 eV include: ^{115}In, ^{177}Hf, and ^{240}Pu.

Moderator Elements with low atomic number that are capable of thermalizing the neutron population and absorbing fission fragment kinetic energy. Common examples include: H and He.

Fertile Fuel Nuclides that undergo neutron induced transmutation into fissile fuel. Also known as breeding material. Common examples include: ^{232}Th for breeding ^{233}U, and ^{238}U for breeding ^{239}Pu.

Transuranic Elements Elements with atomic number (Z) greater than U ($Z > 92$). This definition intentionally includes material that is considered by the US Atomic Energy Act of 1954 [42] to be high-level waste (HLW) and transuranic (TRU) waste.

Fission Products Matter that includes the fission reaction products and anything else not covered by the other ingredients.

The fissile fuel, passive agent, and moderator are essential nanofuel ingredients. The interplay between the essential ingredients is illustrated using plutonium isotope 239 hexafluoride ($^{239}PuF_6$) for the fissile fuel, plutonium isotope 240 hexafluoride ($^{240}PuF_6$) for the passive agent, and molecular hydrogen (H_2) for the moderator. Although sophisticated theoretical and computational models are required to accurately quantify the properties of general nanofuels, for instance the mixture of uranium dioxide (UO_2) and molecular hydrogen (H_2) is an aerosol that behaves as a colloidal system with solid particulates dispersed in a gaseous medium, the nanofuel ingredients explored in this section are accurately modeled as a simple homogeneous gaseous molecular mixture.

Creating a nanofuel comprised of the aforementioned essential ingredients involves a few basic chemical processes, namely:

1. Form plutonium tetrafluoride (PuF_4) or plutonium dioxide (PuO_2) with the desired ratio of fissile fuel to passive agent. The resultant product contains a mixture of plutonium isotopes and can be prepared using existing proliferation resistant UREX+ (uranium reduction extraction) reprocessing techniques. [43]

2. Convert the plutonium mixture into plutonium hexafluoride (PuF_6) using elemental fluorine as the fluorinating or oxidizing agent. The main chemical reactions are:

$$PuF_4 + F_2 \rightarrow PuF_6, \tag{7}$$

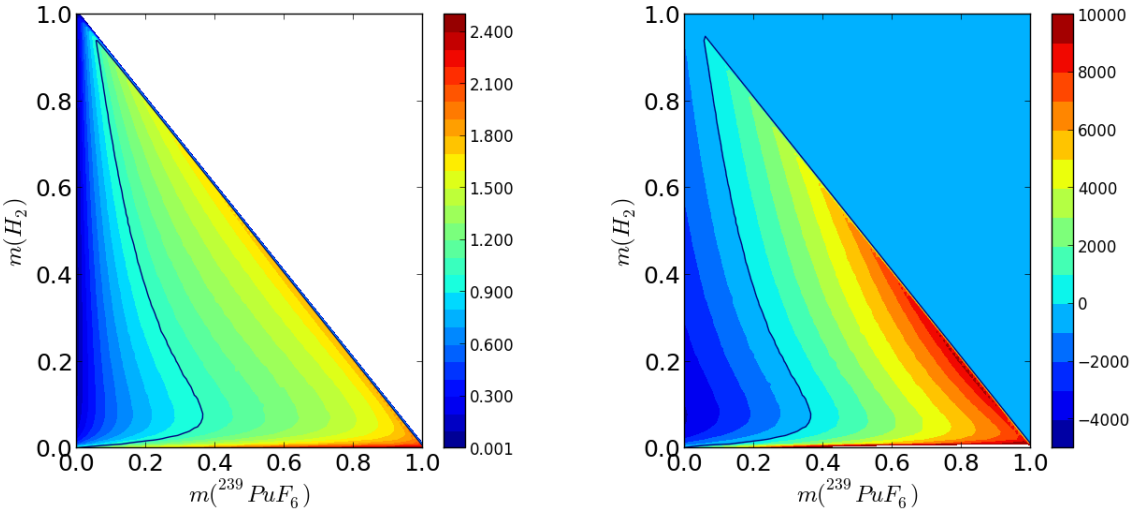
$$PuO_2 + 3F_2 \rightarrow PuF_6 + O_2. \tag{8}$$

   Plutonium hexafluoride has a low melting point temperature (323.9 K at the triple point [44, 45]), which permits low engine intake temperatures.

3. Mix the plutonium hexafluoride with molecular hydrogen until the desired concentration is achieved. Plutonium hexafluoride and molecular hydrogen react on a timescale much longer than a power cycle. [46]

Additional nanofuel ingredients are considered throughout this paper. For instance, Sec. 10 discusses the benefits of fertile fuel, Sec. 7 focuses on the addition of transuranics elements from LWR SNF, and Sec. 6 covers the presence of fission products and the role of delayed neutrons in long-term nanofuel engine operation.

Now let us turn to the numerical calculation of two nanofuel properties that are key to describing a fission chain reaction, namely the infinite medium multiplication factor (k_∞) and the neutron population exponential growth factor (α). First, k_∞ is defined as the



a) k_∞ **b)** α **[1/s]**

Figure 7: **5,151 MCNP5 simulations depicting (a)** k_∞ **and (b)** α **as a function of the nanofuel ingredient mass fractions** m**(H$_2$, ^{239}PuF$_6$, ^{240}PuF$_6$) for a fixed** $\rho = 0.02$ **g/cm^3 and** $T = 800$ **K. The solid black contour corresponds to (a)** $k_\infty = 1$ **and (b)** $\alpha = 0$ **1/s.**

ratio of the neutron population in one generation to the neutron population in the preceding generation in a reactor of infinite extent. [16] When $k_\infty > 1$ ($k_\infty < 1$) the neutron population is increasing (decreasing) and the system is supercritical (subcritical). Second, α is defined by

$$N(t) = N_0 e^{\alpha t}, \tag{9}$$

where N is the neutron population at time t and N_0 is the initial neutron population at time $t_0 = 0$ s. The role of α is to exponentially alter the neutron population. When $\alpha > 0$ 1/s ($\alpha < 0$ 1/s) the neutron population is exponentially increasing (decreasing).

The ensuing simulations use MCNP5 [47] to computationally model neutron-photon-electron transport in systems that contain nuclear material. Simulation input includes: neutron interaction data from the ENDF/B-VII.0 library; photoatomic interaction data and electron interaction data from the 03 libraries; and $S(\alpha, \beta)$ cross-section libraries when appropriate. All simulations use makxsf [48] to create temperature-dependent libraries.

Figure 7 plots k_∞ and α as a function of the nanofuel ingredient mass fractions m(H$_2$, ^{239}PuF$_6$, ^{240}PuF$_6$) for a fixed $\rho = 0.02$ g/cm^3 and $T = 800$ K. In these simulations the system has an infinite extent and the effects of delayed neutrons are neglected. The mass fractions form a convex combination, the abscissa (ordinate) reflects the mass fraction $m(^{239}\text{PuF}_6)$

label	$m(H_2)$	$m(^{239}PuF_6)$	$m(^{240}PuF_6)$	k_∞	α [1/s]
a	0.50	0.34	0.16	1.380	3,173
b	0.50	0.40	0.10	1.478	4,339
c	0.50	0.45	0.05	1.575	5,433
d	0.60	0.27	0.13	1.374	2,554
e	0.60	0.32	0.08	1.476	3,541
f	0.60	0.36	0.04	1.566	4,449
g	0.70	0.21	0.09	1.368	1,989
h	0.70	0.24	0.06	1.450	2,605
i	0.70	0.28	0.02	1.564	3,510

Table 1: **Various nanofuels and their properties at $\rho = 0.02$ g/cm^3 and $T = 879$ K.**

($m(H_2)$), and the mass fraction $m(^{240}PuF_6)$ mass fraction is found from

$$m(^{240}PuF_6) = 1 - m(H_2) - m(^{239}PuF_6). \tag{10}$$

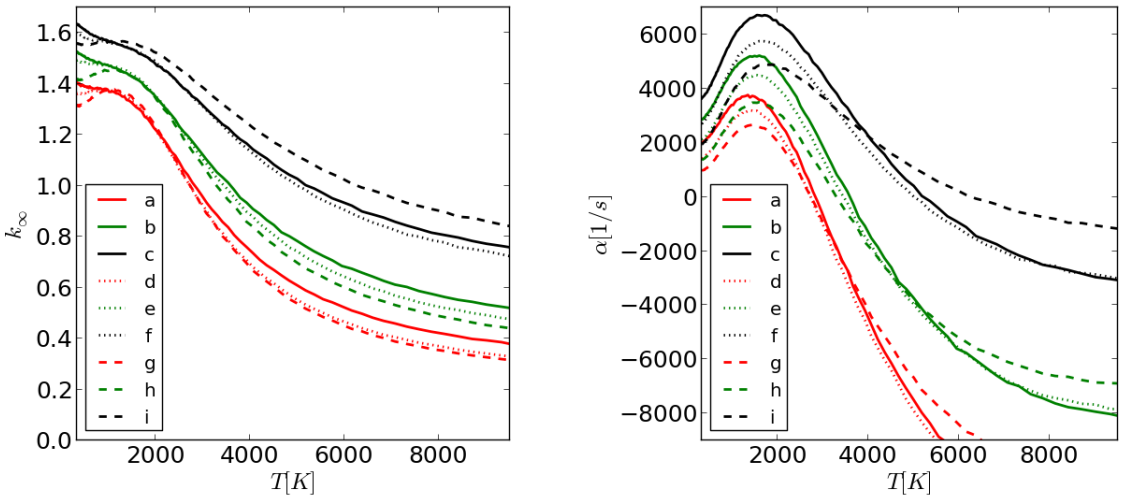
There are $n = 101$ data points in each dimension and the figure contains $n(n+1)/2 = 5,151$ simulation results.

Figure 7a illustrates a large range of supercritical ($k_\infty > 1$) nanofuels. Almost the entire moderator mass fraction domain can support a fission chain reaction. Figure 7a also shows that $k_\infty > 2$ for small values of $m(H_2)$ and $m(^{240}PuF_6)$ (or large values of $m(^{239}PuF_6)$), which is not obvious given the abundance of F atoms present in the nanofuel. Table 1 reports k_∞ and α for 9 nanofuels with moderator mass fractions in $[0.5, 0.6, 0.7]$ and k_∞ approaching $[1.4, 1.5, 1.6]$ for a fixed nanofuel $\rho = 0.02$ g/cm^3 and $T = 879$ K. Figure 7b and Table 1 show that a majority of the supercritical nanofuels have an α on the order of a few times 10^3 1/s. In particular, for Fuel c: $k_\infty = 1.575$ and $\alpha = 5,433$ 1/s.

Another important nanofuel property is the temperature coefficient of reactivity (α_T), which is given by

$$\alpha_T = \frac{\partial}{\partial T}\left(\frac{k-1}{k}\right) = \frac{1}{k^2}\frac{\partial k}{\partial T}, \tag{11}$$

where k is the neutron multiplication factor. Since k is a positive number, the sign of α_T is proportional to the derivative of k with respect to T ($k'(T)$). Negative (positive) α_T describes a decrease (an increase) in k with an increase in T. Figure 8 plots k_∞ and α as a function of T, for the nanofuels identified in Table 1 and a fixed $\rho = 0.02$ g/cm^3, and shows that $k'(T) < 0$ 1/K across a large temperature domain. For example, Fuel c has a negative α_T across the entire temperature domain plotted.



a) $k_\infty(T)$ **b)** $\alpha(T)$ **[1/s]**

Figure 8: **900 MCNP5 simulations depicting (a)** k_∞ **and (b)** α **as a function of** T **for the nanofuels identified in Table 1 and a fixed** $\rho = 0.02$ **g/cm**^{3}**.**

Nanofuels with negative α_T are inherently stable. [49] This is an important safety feature. According to the Nordheim-Fuchs model, in systems where the effects of delayed neutrons and heat transfer can be neglected, nuclear fuels with a negative α_T undergo a self-limiting power excursion (or burst) with a burst duration $\tau_b \sim 4/\alpha$. [50] Therefore, in a power cycle a nanofuel with a negative α_T ensures a finite release of nuclear energy.

Now let us turn to the ideal Otto cycle combustion process for nanofuels with a negative α_T. This process involves the following intermediate stages:

1. In state 2 the nanofuel is supercritical ($k > 1$) and the injection of neutrons starts an exponential growth in the neutron population according to Eq. 9.

2. The nuclear energy production rate is proportional to the neutron population. As the neutron population exponentially increases: the fissile fuel fissions and releases nuclear energy; the moderator absorbs the fission fragment kinetic energy, which accounts for approximately 80% of the total energy released in a fission reaction [16]; and the nanofuel temperature increases.

3. For negative α_T, k decreases as T increases and the nanofuel undergoes a critical transition. When the nanofuel is subcritical ($k < 1$) the neutron population and the nuclear energy production rate decrease exponentially.

4. In state 3 the nanofuel is subcritical ($k < 1$), the neutron population and the nuclear energy production rate are negligible, and the combustion process ends.

The physical explanation for the nanofuel negative α_T involves the strong resonance neutron absorption cross-section in the passive agent. As the neutrons collide with the moderator, the neutron velocity distribution function rapidly relaxes toward a Maxwellian velocity distribution characterized by the macroscopic nanofuel properties. As the nanofuel temperatures increases, the neutron velocity distribution function broadens and there are more neutrons with energies near the passive agent neutron resonance absorption cross-section. This capture mechanism creates a neutron sink that significantly increases with the nanofuel temperature.

4 Engine core criticality

Neutrons propagate a fission chain reaction. Criticality calculations account for the neutron source (fission reaction) and sink (capture and leakage) terms in a fission chain reaction. This section performs theoretical one-speed diffusion theory criticality calculations to estimate the critical size of an engine (reactor) core in a reciprocating nanofuel internal engine. This section also discusses the second nanofuel engine inherent safety feature, which pertains to the dynamic engine core geometry.

Let us begin by identifying an engine core geometry that minimizes neutron leakage. The engine core in a reciprocating internal engine (see Fig. 2) is a right circular cylinder with fixed radius (R) and variable height (H).

Neutron leakage is proportional to the ratio of the engine core surface ($S = 2\pi R(R+H)$) to the engine core volume ($V = \pi R^2 H$):

$$\frac{S}{V} = \frac{2}{R} + \frac{2}{H}. \tag{12}$$

To minimize the engine core surface-to-volume ratio: consider a unit volume $V = \pi R^2 H = 1$; let $H = xR$, where x is the quantity to be determined; and look for solutions where the derivative vanishes. Performing these steps: $R = (\pi x)^{-1/3}$; $f(x) = S/V = 2\pi^{1/3} x^{-2/3}(1+x)$; $f'(x) = \frac{2}{3}\pi^{1/3}(x-2)x^{-5/3}$; and the pertinent solution is $x = 2$. Thus, $H = 2R$ minimizes neutron leakage and defines an optimal engine core geometry with volume $V = 2\pi R^3$. This solution makes the cylinder closest to being a sphere.

For optimal engine core geometries, let us calculate the engine core critical radius using the one-speed diffusion theory general criticality condition. Assume the engine core contains a

label	L [cm]	D [cm]	Σ_a [1/m]	$\tilde{R}_c$ [cm]	R_c [cm]	M_c [kg]
a	13.14	1.186	0.6869	61.23	58.70	25.42
b	13.14	1.180	0.6834	54.59	52.08	17.75
c	13.14	1.174	0.6800	49.77	47.27	13.27
d	12.66	1.006	0.6277	59.46	57.32	23.66
e	12.66	1.002	0.6252	52.71	50.57	16.25
f	12.67	0.9988	0.6222	48.37	46.25	12.43
g	12.39	0.8724	0.5683	58.67	56.81	23.04
h	12.40	0.8707	0.5663	53.10	51.24	16.91
i	12.41	0.8683	0.5638	47.47	45.61	11.93

Table 2: **Critical engine core characteristics for the nanofuels identified in Table 1.**

homogeneous gaseous nanofuel surrounded by a vacuum. The general criticality condition is given by

$$B_m^2 = B_g^2, \tag{13}$$

where B_m^2 is the material buckling (nanofuel properties) and B_g^2 is the geometric buckling (engine core geometry).

The material buckling is determined by the nanofuel properties:

$$B_m^2 = \frac{k_\infty - 1}{L^2}, \tag{14}$$

where $L = \sqrt{D/\Sigma_a}$ is the neutron diffusion length (a measure of how far a neutron will travel from its source before it is absorbed), D is the neutron diffusion coefficient, and Σ_a is the macroscopic neutron absorption cross-section. The geometric buckling is determined by the engine core geometry:

$$B_g^2 = \left(\frac{\nu_0}{\tilde{R}_c}\right)^2 + \left(\frac{\pi}{\tilde{H}_c}\right)^2, \tag{15}$$

where $\nu_0 = 2.40483$ is the first zero of the Bessel function of the first kind ($J_0(x)$) and $\tilde{R}_c$ ($\tilde{H}_c$) is the extrapolated critical radius (height). The slab geometry extrapolated distance (d) with a vacuum boundary condition is

$$d = 0.7104\lambda_{tr} = 2.131D, \tag{16}$$

where $\lambda_{tr} = 3D$ is the neutron transport mean free path. [16]

To find the critical radius: substitute Eq. 14 (material buckling) and Eq. 15 (geometric buckling) into Eq. 13 (general criticality condition); set $H = 2R$ (optimal engine core geometry); solve for the extrapolated critical radius; and subtract the extrapolation distance.

The extrapolated critical radius is

$$\tilde{R}_c = \sqrt{\frac{L^2}{k_\infty - 1}\left(\nu_0^2 + \frac{\pi^2}{4}\right)}. \tag{17}$$

The critical radius (mass) is $R_c = \tilde{R}_c - d$ ($M_c = \rho V = \rho 2\pi R_c^3$). Table 2 presents the critical radius (mass) for the nanofuels identified in Table 1. In particular, Fuel c has $R_c = 47.27$ cm, $M_c = 13.27$ kg, and $M_c(^{239}\mathrm{PuF_6}) = 5.972$ kg.

This result estimates the minimum size of an engine core. However, in a reciprocating internal engine the engine core height varies as the piston oscillates in the cylinder and the criticality changes. To explore this effect let us introduce a variable compression ratio ($\mathfrak{r}$). During the compression stroke $\mathfrak{r}$ is defined by

$$\mathfrak{r} = \frac{H_1}{H}, \tag{18}$$

where $\mathfrak{r} = 1$ ($\mathfrak{r} = r$) in state 1 (state 2).

To find the critical radius in a variable engine core geometry: define H_c in terms of $\mathfrak{r}$ ($H_c = H_1/\mathfrak{r}$), which accounts for the change in engine core volume; let $L = L_1/\mathfrak{r}$, since the neutron diffusion length is proportional to the nanofuel density; set $H_c = 2R_c$ (optimal engine core geometry); solve for the extrapolated critical radius; and subtract the extrapolation distance. The result is

$$R_c = \frac{\nu_0}{\mathfrak{r}}\left\{\frac{k_\infty - 1}{L_1^2} - \frac{\pi^2}{(H_1 + 2d\mathfrak{r})^2}\right\}^{-1/2} - d. \tag{19}$$

This expression shows that $R_c \sim 1/\mathfrak{r}$. In particular, for Fuel c, expanding Eq. 19 in $\mathfrak{r}$ gives

$$R_c[\mathrm{cm}] \cong \frac{509.7}{\mathfrak{r}} - 3.840 + 0.01589\mathfrak{r} - O(\mathfrak{r}^2), \tag{20}$$

where $H_1 = 945.4$ cm and the initial critical mass is $M_c = 1,627$ kg.

This surprisingly large initial critical radius (enormous initial critical mass) is the primary reason why gaseous nuclear technology has not been heavily explored. The scaling is easy to explain using a column density argument. The column density in spherical geometry is ρR_s, where R_s is the spherical radius. In order to maintain a critical spherical assembly, any change in ρ must be balanced by a change in R_s in such a way that ρR_s remains constant. For transitions from state a to state b, this column density argument implies the following scaling:

$$M_b = M_a\left(\frac{\rho_a}{\rho_b}\right)^2, \tag{21}$$

$$V_b = V_a\left(\frac{\rho_a}{\rho_b}\right)^3. \tag{22}$$

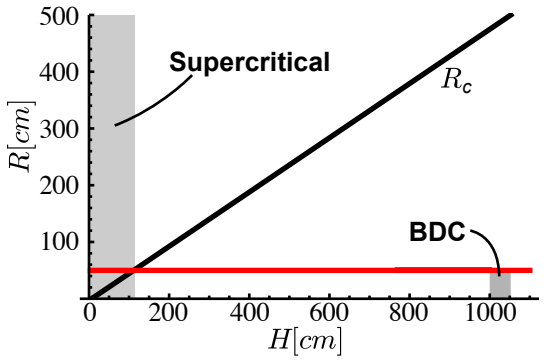


Figure 9: **Engine core critical radius for Fuel c (in Tables 1 and 2) as a function of piston position. The horizontal (red) line represents the engine core radius.**

Thus, in transitioning from a solid fuel to a gaseous fuel, the density decreases by 10^{-3} and the critical mass (volume) increases by 10^6 (10^9). Stating the obvious, increasing the reactor volume by a factor of 10^9 incurs a significant cost.

Conversely, in a nanofuel engine this scaling has an advantage. As the piston moves from state 1 (BDC) to state 2 (TDC), the nanofuel density increases by a factor of r and the nanofuel critical mass decreases by a factor of r^2. In designing a nanofuel engine, the engine core radius is intentionally selected to ensure that the critical radius is less than the engine core radius only when the piston is near the TDC crank position. In other words, a nanofuel engine is only supercritical ($R > R_c$) when the piston is near the TDC crank position. In particular, for Fuel c, Fig. 9 illustrates this concept using $H_1 = 1,000$ cm and $R = 50$ cm. This engine forms a critical assembly when $H = 107.6$ cm, which is near the optimal TDC crank position of $H_2 = 100$ cm.

The effect of the variable or dynamic engine core geometry on criticality is second important inherent safety feature of nanofuel engines. First, since the engine core is subcritical ($R < R_c$) during a majority of the Otto cycle, an accidental injection of neutrons or the presence of background neutrons has little effect on the neutron population. The spurious neutrons will simply exponentially decay in time. Second, in a power cycle the change in engine core volume is another means of placing an upper limit on the release of nuclear energy. Energy production ceases once the engine core volume is too large. As the engine core volume increases, ρ decreases and the neutron leakage increases.

5 Ideal engine performance

The previous two sections followed a traditional nuclear engineering approach to studying the behavior of a nanofuel (nuclear fuel) in a reciprocating internal engine (configuration designed to support a fission chain reaction). This section returns to the ideal Otto cycle and models nanofuel engine performance.

The ideal Otto cycle processes for a reciprocating nanofuel engine are:

Intake During the intake process the nanofuel must be in the gaseous phase, which sets a lower bound on the temperature at any given state. The Otto cycle begins in state 1, where the piston is located in the BDC crank position and a mass of nanofuel (M) is confined within an engine core of volume $V_1 = \pi R^2 H_1$.

Compression During process 1-2 the nanofuel is isentropically compressed. The system forms a critical assembly before reaching state 2. This occurs for a bare (no reflector) engine core when $R = R_c$, where R_c is given by Eq. 19. In state 2, the piston is located in the TDC crank position, the system is supercritical, and the nanofuel properties are given by: $\rho_2 = r\rho_1$, $T_2 = r^{\gamma-1}T_1$, and $p_2 = r^{\gamma}p_1$.

Combustion During process 2-3 the nanofuel internal energy increases at constant volume. This process begins when neutrons are introduced into the system and ends due to the nanofuel negative α_T. In state 3, the nanofuel temperature (T_3) and pressure (p_3) attain maximum values.

Expansion During process 3-4 the nanofuel isentropically expands and the piston drives the crankshaft. In state 4, the piston is in the BDC crank position.

Exhaust During the exhaust process the nanofuel exits the engine.

In a non-ideal nanofuel engine the Otto cycle combustion process does not occur at constant volume. It starts when neutrons are present in a supercritical system, which occurs before the piston reaches the TDC crank position. It can end when the engine core volume increases and the system turns subcritical, due to decrease in ρ and an increase in neutron leakage. This occurs for a bare core when $R < R_c$, where R_c is given by Eq. 19.

Neutrons are introduced into the system using either an external or an internal neutron source. Analogous to the ignition methods in internal-combustion engines that release chemical energy, **spark-ignition** refers to the use of an external neutron source and **compression-ignition** refers to the use of an internal neutron source. In general, both external and internal sources can include any radioactive material that emits neutrons.

label	Q [MJ]	T_3 [K]	p_3 [bar]	$\sigma_{\theta\theta}$ [bar]	α_2 [1/s]	τ_b [ms]
a	436.0	2,997	1,243	2,603	246.5	16.23
b	427.3	4,730	1,553	3,014	324.2	12.34
c	483.0	4,988	2,069	3,787	398.4	10.04
d	398.8	2,664	1,323	2,728	193.0	20.73
e	423.4	3,514	1,746	3,328	281.4	14.21
f	490.4	4,666	2,318	4,189	336.5	11.89
g	456.4	2,686	1,555	3,188	142.1	28.15
h	455.2	3,258	1,886	3,623	202.1	19.79
i	602.1	5,005	2,898	5,195	261.0	15.32

Table 3: **Nanofuel engine ideal Otto cycle combustion process simulations for the nanofuels identified in Table 1 and the critical dimensions presented in Table 2.**

Two classes of pulsed fusion neutron generators are ideal for spark-ignition:

1. Accelerator-based neutron generators are a mature technology and commercial products are readily available. For example, the All-Russia Research Institute of Automatics ING-013 produces 10^8 neutrons within 0.8 μs and has an operating lifetime of 3.6×10^5 shots. [51] A similar product is the Activation Technology Corporation N550, which produces 10^8 neutrons within 10 μs. [52]

2. Z-pinch-based dense plasma focus (DPF) [53–55] neutron generators offer an energy efficient and cost effective means of performing nuclear fusion. For example, Michel *et al.* [56] experimentally demonstrated a neutron yield $Y \sim 2.8 \times 10^8$ using molecular deuterium (D_2) and a driver with energy (voltage) 1.35 kJ (20 kV). In addition, Decker *et al.* [57, 58] experimentally demonstrated that fast (400 ns rise time) high-impedance (60 mΩ) drivers increase the ratio of neutron yield to driver energy (Y/kJ).

Pulsed fusion neutron generators have an operating lifetime of 10^5 shots, due to the capacitor lifetime. For a spark-ignition nanofuel engine operating at 1 cycle per second (cps), this requires replacing the neutron generator on a daily basis. Alternatively, after a minute of spark-ignition engine operation, fission product delayed neutrons provide a natural internal neutron source and allow a transition to compression-ignition engine operation.

Now let us turn to the numerical calculation of the ideal Otto cycle combustion process. The following simulations use a self-consistent time-dependent Lagrangian hydrodynamics and Monte Carlo neutron-photon-electron transport model. The Lagrangian hydrodynamics model uses second-order discretizations [59–61]; the Monte Carlo transport model is MCNP5 [47].

Nanofuel engine simulation initialization includes:

1. Set the nanofuel properties in state 1: $\rho_1 = 0.002$ g/cm^3 and $T_1 = 350$ K.
2. For isentropic compression ($r = 10$) of an ideal gas ($\gamma = 1.4$), the nanofuel properties in state 2 are: $\rho_2 = 0.02$ g/cm^3 and $T_2 = 879$ K.
3. Set $H_2 = 2R$ (optimal engine core geometry) to minimize neutron leakage from the engine core when the piston is in the TDC crank position.
4. Surround the engine core with a 40 cm thick Be neutron reflector ($T = 800$ K) to further reduce neutron leakage (see App. A). The reflector includes both the piston case and the piston itself.
5. Inject 10^8 fusion (14 MeV) neutrons into the engine core over 1 μs. This starts the combustion process, which ends due to the nanofuel negative α_T.

Table 3 presents the simulation results for the nanofuels identified in Table 1 and the critical dimensions presented in Table 2. Q is the energy absorbed in the nanofuel during the combustion process; T_3 (p_3) is the nanofuel temperature (pressure) in state 3; $\sigma_{\theta\theta}$ is the maximum hoop stress at the piston case inner surface (see App. B); α_2 is the neutron population exponential growth factor in state 2; and $\tau_b = 4/\alpha_2$ is the Nordheim-Fuchs burst duration. In particular, for Fuel c: $Q = 483.0$ MJ; $T_3 = 4,988$ K ($p_3 = 2,069$ bar); $\sigma_{\theta\theta} = 3,787$ bar; $\alpha_2 = 398.4$ 1/s; and $\tau_b = 10.04$ ms.

The ideal Otto cycle efficiency is $\eta = 60.19\%$. For a nanofuel engine operating at 1 cps, the Fuel c ideal engine performance metrics include: net work per cycle $W = 290.7$ MJ; engine power $P = 290.7$ MW (3.899×10^5 hp); and electric power output $P_e = 284.9$ MW$_e$ (assuming 98% generator efficiency). This is an efficient nuclear reactor. In general, these results are consistent with experimental data from a number of reactor safety tests and pulsed reactor systems. [50]

6 Engine performance

Numerous design factors affect nanofuel engine performance. Engine design involves optimizing the economics, size, weight, power, durability, reliability, efficiency, life expectancy, and many other factors for a particular application. Before designing a nanofuel engine for an electric power plant, this section models the performance of a generic 4-stroke reciprocating nanofuel engine operating in spark-ignition and compression-ignition mode.

For both ignition methods, nanofuel engine simulation initialization includes:

1. Select the nanofuel given by Fuel c in Table 1.
2. Set the nanofuel properties in state 1: $\rho_1 = 0.002$ g/cm^3 and $T_1 = 350$ K.
3. Assign the engine core dimensions: $R = H_1/20 = 50$ cm. These dimensions form the optimal engine core geometry ($H = 2R$) when $r = 10$.
4. Surround the engine core with a 40 cm thick Be neutron reflector ($T = 800$ K), which includes both the piston case and the piston itself.

The piston dynamics and engine core height are treated as a moving boundary condition that evolves in time according to

$$H(t) = (l_r + l_c + 2R) + l_c \cos(\text{cps}4\pi t) - \sqrt{l_r^2 - l_c^2 \sin^2(\text{cps}4\pi t)}, \tag{23}$$

where l_r (l_c) is the connecting rod (crank) length (see Fig. 2). The following nanofuel engine simulations use $l_r = 18$ m and $l_c = 4.5$ m.

6.1 Spark-ignition mode

Spark-ignition is the preferred method of starting a nanofuel engine. Figure 10 illustrates the simulation geometry and piston dynamics of a 4-stroke reciprocating nanofuel engine operating at 1 cps. The piston reaches the TDC crank position (quarter cycle) and the engine core attains the minimum surface-to-volume ratio ($H_2 = 2R = 100$ cm) at $t = 250$ ms. The system forms a critical assembly at $t = 146.1$ ms ($H = 485.2$ cm, $\mathfrak{r} = 2.061$). Compared to the bare engine core example in Sec. 4, where the system formed a critical assembly at $H = 107.6$ cm, the neutron reflector significantly decreases the critical radius (size) of the engine core for given mass of nanofuel.

The spark time (t_s) is the time when the pulsed fusion neutron generator is fired and neutrons are injected into the system. The optimal spark time maximizes torque. In spark-ignition mode, where the main objective is to start the engine and allow fission product delayed neutrons to accumulate, it is sufficient to ensure the peak nanofuel pressure occurs after the piston reaches the TDC crank position. Since there is little neutron population amplification near the critical transition, this nanofuel engine simulation set $t_s = 175$ ms ($H = 322.7$ cm, $\mathfrak{r} = 3.099$) and injected 10^8 fusion (14 MeV) neutrons into the system within 1 μs.

Spark-ignition nanofuel engine simulation results include: $Q = 613.1$ MJ, $\xi = 20.92$, $T_3 = 5,078$ K, and $p_3 = 1,870$ bar. For comparison, the equivalent ideal Otto cycle combustion process simulation results are: $Q = 622.5$ MJ, $\xi = 21.24$, $T_3 = 5,274$ K, and

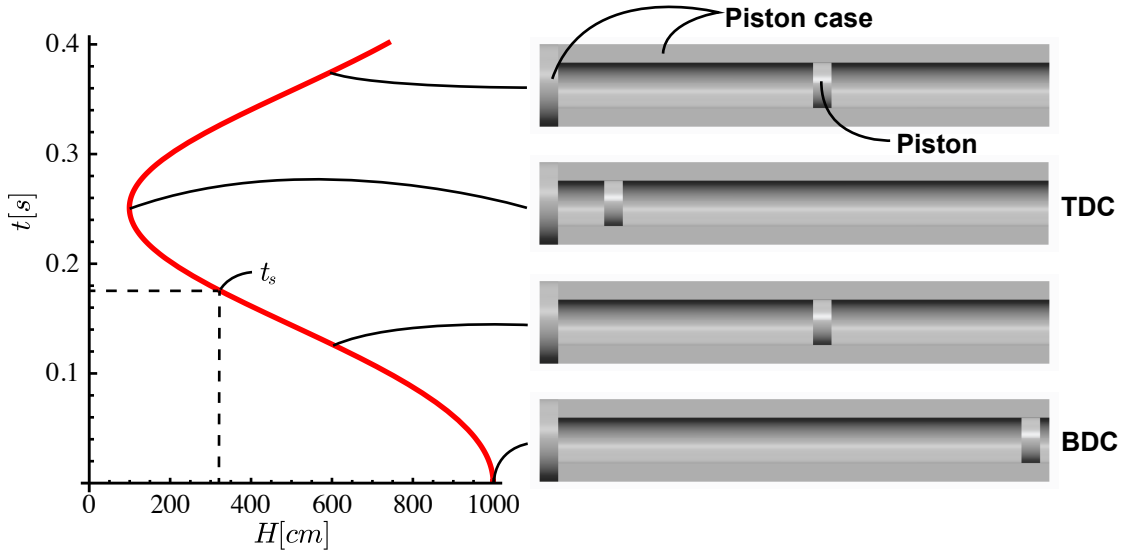


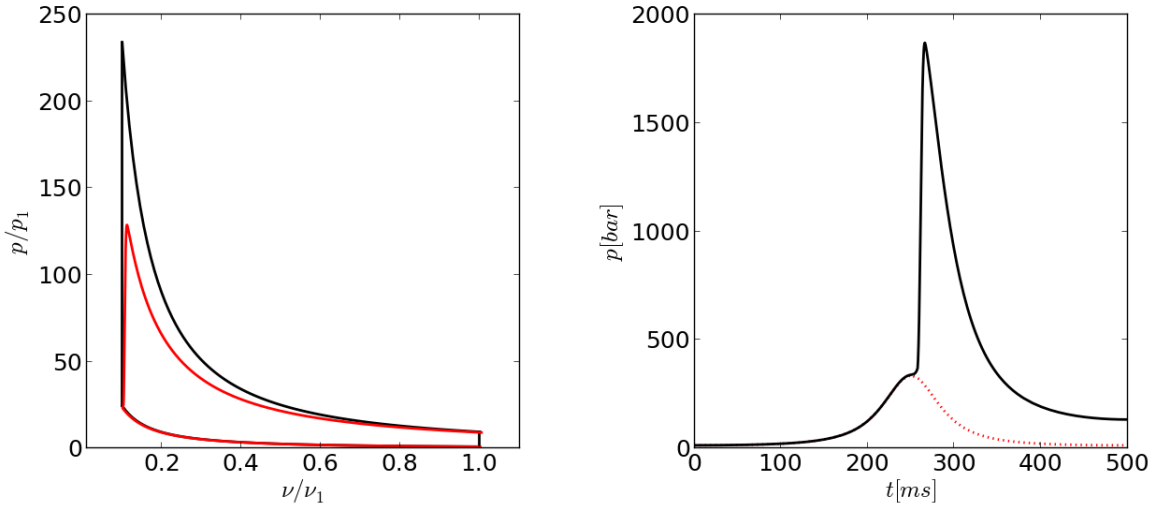
Figure 10: **Simulation geometry and piston dynamics of a 4-stroke reciprocating nanofuel engine ($l_r = 18$ m, $l_c = 4.5$ m) operating at 1 cps.**

$p_3 = 2,188$ bar. In the non-ideal simulation the engine core spends more time away from the optimal geometry, which increases the neutron leakage and decreases the peak nanofuel properties.

Maintaining the structural integrity of the material surrounding the engine core sets an upper limit on the peak nanofuel properties, and hence the maximum energy released per power cycle. It is undesirable to allow any portion of the piston case or piston to melt or undergo plastic deformation. Compared to a fossil-fuel based internal-combustion engine, a nanofuel engine has similar heat transfer characteristics (heat flux, thermal stress) and higher intake fuel pressures (to reduce engine core size). To study the effect of this pressure increase, App. B uses the theory of elasticity to calculate the piston case deformation due to the nanofuel pressure. The piston case will undergo elastic deformation provided the hoop stress at the inner surface of the piston case is below 90% of the material yield strength.

From Eq. 67 (Eq. 68) the hoop stress (deflection) at the inner surface of the piston case is $\sigma_{\theta\theta} = 3,540$ bar ($u = 670.3\mu$m); from Eq. 69 the Be yield strength is $\sigma_y(800\text{K}) = 2,114$ bar; and the peak nanofuel pressure limit is $p_{\max} \lesssim 1005$ bar. In this engine simulation: $p_3 > p_{\max}$. Although $\sigma_{\theta\theta} > \sigma_y(800\text{K})$, the hoop stress drops below the Be yield strength at $R = 72.70$ cm or 22.70 cm into the reflector.

Aside from limiting the energy released per power cycle, there are two engineering approaches to improving the structural integrity of a nanofuel engine. First, applying an external pressure of $p_{out} = 565.9$ bar to the piston case outer surface reduces the hoop stress at the inner



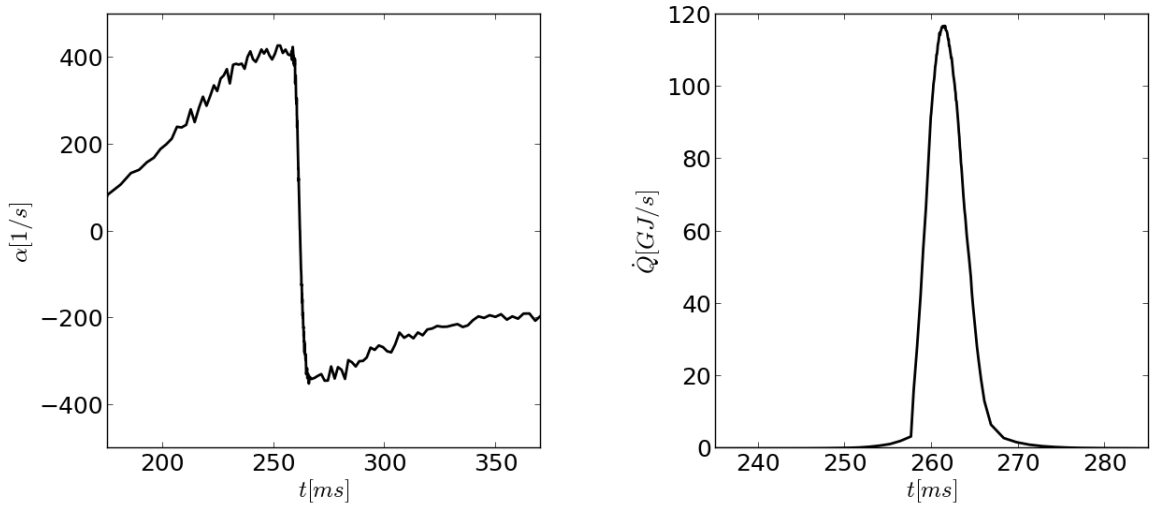
a) Otto cycle **b) p [bar]**

Figure 11: **Spark-ignition reciprocating nanofuel engine simulation. (a) Simulated (red) and ideal (black, $r = 10$, $\xi = 20.92$, and $\gamma = 1.389$) Otto cycle. (b) Nanofuel (black) and motored (dashed red) p as a function of time.**

surface of the piston case to 90% of the Be yield strength. With this applied pressure the deflection at the inner surface of the piston case is $u = 365.6\mu$m. Second, cooling the piston case to $T = 400$ K ($T = 600$ K) increases the Be yield strength to $\sigma_y(400\text{K}) = 3,541$ bar ($\sigma_y(600\text{K}) = 2,788$ bar).

Figure 11a compares the simulated and ideal ($r = 10$, $\xi = 20.92$, and $\gamma = 1.389$) Otto cycles. In particular, the simulated (ideal) nanofuel engine efficiency is $\eta = 38.23\%$ (59.17%). General spark-ignition engine performance metrics include: net work per cycle $W = 234.4$ MJ; engine power $P = 234.4$ MW (3.138×10^5 hp); and electric power output $P_e = 229.7$ MW$_e$ (assuming 98% generator efficiency). Figure 11b illustrates the increase in nanofuel pressure during the combustion process compared to the motored pressure, which is the pressure in an engine that does not release energy. Nuclear energy is clearly absorbed in the working fluid and the peak pressure occurs at $t = 266.0$ ms, which is after the quarter cycle time.

In a conventional spark-ignition engine the fuel-air mixture combustion process is initiated by an electric discharge. A deflagration front starts at the initiation point and propagates through the fuel-air mixture until it reaches the engine core surface. In a spark-ignition nanofuel engine a deflagration front does not exist. Instead, the combustion process is initiated by the injection of fast fusion neutrons into the system. Fast neutrons rapidly escape the engine core and are thermalized in the reflector; thermal neutrons diffuse into the



a) α **[1/s]** **b)** $\dot{Q}$ **[GJ/s]**

Figure 12: **Spark-ignition reciprocating nanofuel engine simulation depicting (a)** α **1/s and (b)** $\dot{Q}$ **GJ/s as a function of time.**

engine core from all reflector surfaces and propagate the fission chain reaction. Simulation results show that thermal (fast) neutrons account for more than 95% (less than 0.5%) of the fissions. This nanofuel engine combustion process exhibits uniform volumetric heating of the working fluid and allows scaling to high-power single-cylinder engines.

Figure 12a plots α as a function of time. During the compression stroke α increases as the nanofuel density increases; α rapidly decreases due to the nanofuel negative α_T; and during the expansion stroke α slightly increases as the nanofuel temperature decreases. Figure 12b plots the nanofuel energy absorption rate ($\dot{Q}$) as a function of time. According to the Nordheim-Fuchs model, the burst duration is approximately $\tau_b = 4/\alpha \sim 4/400$ s ~ 10 ms. This curve can be approximated by a square wave function of height $\dot{Q} \sim 58.4$ GJ/s (half-max) and duration $\tau_b \sim 10$ ms, thereby absorbing $Q \sim 584$ MJ. This estimate is close to the spark-ignition simulation result $Q = 613.1$ MJ.

6.2 Compression-ignition mode

Compression-ignition is the preferred method of long-term nanofuel engine operation. During spark-ignition engine operation, fission product delayed neutrons accumulate and after about a minute they provide a sufficient internal neutron source (S_N) for compression-ignition engine operation.

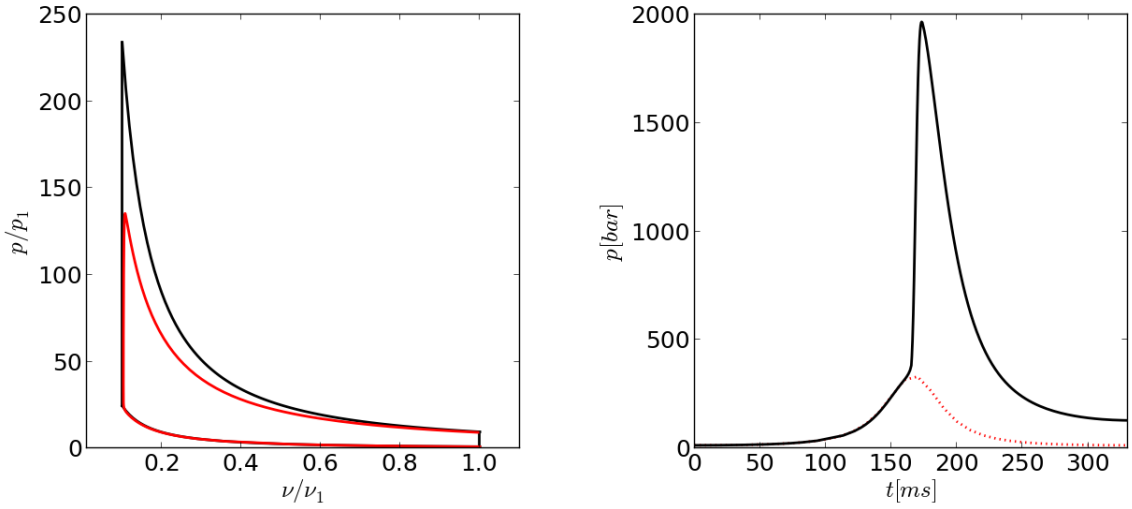
In the previous spark-ignition nanofuel engine simulation the initial mass of nanofuel contained $N_0 = 1.206 \times 10^{25}$ fissile fuel ($^{239}PuF_6$) molecules and the power cycle produced $N_f = 2.410 \times 10^{19}$ fissions, assuming the effective energy released per ^{239}Pu fission is 198.5 MeV/f and 80% of this energy is deposited in the nanofuel [16]. Therefore, only a small fraction of the fissile fuel is depleted during the power cycle ($N_f/N_0 = 1.999 \times 10^{-6}$) and the initial mass of nanofuel contains fissile fuel for several power cycles (5.003×10^5 cycles assuming complete utilization).

Thermal neutron-induced ^{239}Pu fission produces 0.0061 delayed neutrons distributed over several precursor groups with half-lives less than 60 s. [62] Therefore, retaining 1% of the exhaust (nanofuel) in the engine core provides an internal neutron source of $S_N \sim 2.450 \times 10^{13}$ N/s. An internal neutron source of $S_N = 10^{14}$ N/s can be maintained by retaining 4.081% of the exhaust through orificing, which is the process of adjusting the nanofuel intake and exhaust properties.

Since the nanofuel properties in state 1 and the variable compression ratio are set by the simulation initial conditions, maximum torque is obtained by adjusting the operating speed to 1.5 cps. Compression-ignition nanofuel engine simulation results include: $Q = 614.1$ MJ, $\xi = 20.95$, $T_3 = 5,106$ K, and $p_3 = 1,966$ bar. At these operating conditions: S_N is maintained by retaining 2.716% of the exhaust in the engine core; and the nanofuel properties in state 1 are maintained by reducing the intake nanofuel mass flow rate and temperature.

Figure 13a compares the simulated and ideal ($r = 10$, $\xi = 20.95$, and $\gamma = 1.389$) Otto cycles. In particular, the simulated (ideal) nanofuel engine efficiency is $\eta = 43.22\%$ (59.17%). Compression-ignition engine performance metrics include: net work per cycle $W = 265.4$ MJ; engine power $P = 398.1$ MW (5.339×10^5 hp); and electric power output $P_e = 390.1$ MW$_e$ (assuming 98% generator efficiency). Figure 13b illustrates the increase in nanofuel pressure during the combustion process compared to the motored pressure. The nanofuel pressure begins to depart from the motored pressure before the quarter cycle time ($t = 166.7$ ms) and peaks at $t = 173.1$ ms.

Figure 14 plots several system properties as a function of time from the compression-ignition reciprocating nanofuel engine simulation. Figures 14a (k_{eff}) and 14b (α) show that the system turns critical ($k_{eff} = 1$, $\alpha = 0$ 1/s) at $t = 98.23$ ms. Figure 14c (N) shows that the neutron population does not exponentially amplify until the system turns critical. It also shows that the neutron population peaks at $t = 169.0$ ms, which is 70.77 ms after the system turns critical. Figure 14d shows that most of the nuclear energy is absorbed in the nanofuel (working fluid) within a 10 ms window around the neutron population peak.



a) Otto cycle **b) p [bar]**

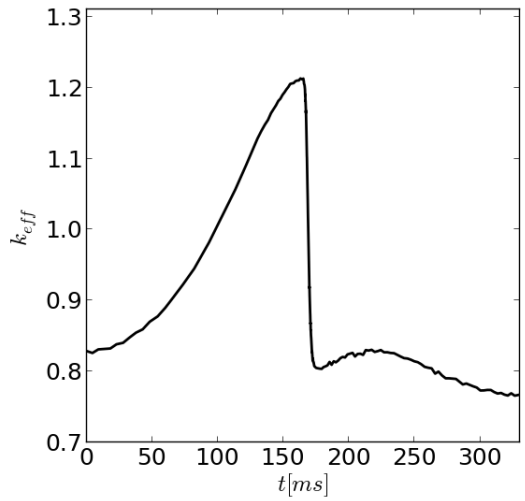
Figure 13: **Compression-ignition reciprocating nanofuel engine simulation. (a) Simulated (red) and ideal (black, $r = 10$, $\xi = 20.95$, and $\gamma = 1.389$) Otto cycle. (b) Nanofuel (black) and motored (dashed red) p as a function of time.**

In a nanofuel engine the combustion process significantly overlaps the compression and expansion strokes. Although a majority of the nuclear energy absorbed in the working fluid during the combustion process occurs in a short period of time (10 ms), the entire combustion process occurs over a much longer period of time (140 ms). This latter time-scale affects the nanofuel engine operating speed.

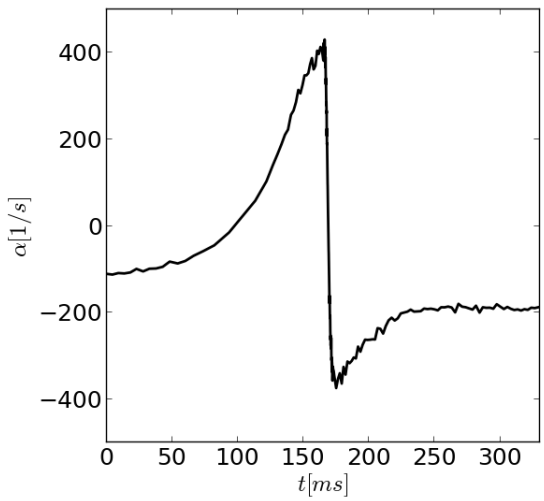
Figure 14d shows that the exhaust contains a substantial amount of energy. In particular, the heat lost from the system is $Q_{41} = -348.7$ MJ. Converting half this energy into useful work can boost the total system efficiency ($\eta > 70\%$).

7 LWR SNF nanofuel

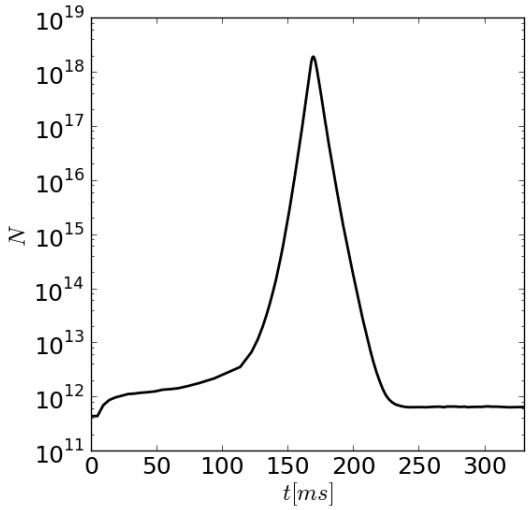
The UREX+ (uranium reduction extraction) process offers several proliferation resistant options for commercial light-water reactor (LWR) spent nuclear fuel (SNF) treatment. In particular, the UREX+1a process separates the transuranic elements, which are the primary long-term dose rate contributors in nuclear waste, in a single product stream. [43] Transmuting (or otherwise eliminating) these elements reduces the volume and radiotoxicity of nuclear waste. This section explores nanofuels comprised of the transuranic elements from LWR SNF and their performance in a nanofuel engine.



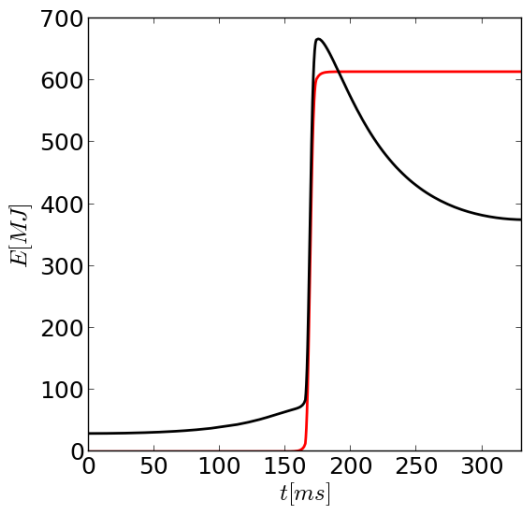
a) k_{eff}



b) α **[1/s]**



c) N



d) U **[MJ] (black) and** Q **[MJ] (red)**

Figure 14: **Compression-ignition reciprocating nanofuel engine simulation depicting several system properties as a function of time.**

Creating a nanofuel comprised of the transuranic elements from LWR SNF involves a few basic chemical processes, namely:

1. Form a tetrafluoride mixture of the transuranic elements (NpF_4, PuF_4, and AmF_4), which can be accomplished thorough one or more UREX+ modules. The resultant product includes fissile fuel ($^{239}PuF_4$), passive agent ($^{240}PuF_4$), and transuranic elements (everything else). The ratio of fissile fuel to passive agent is determined by the LWR SNF feedstock.

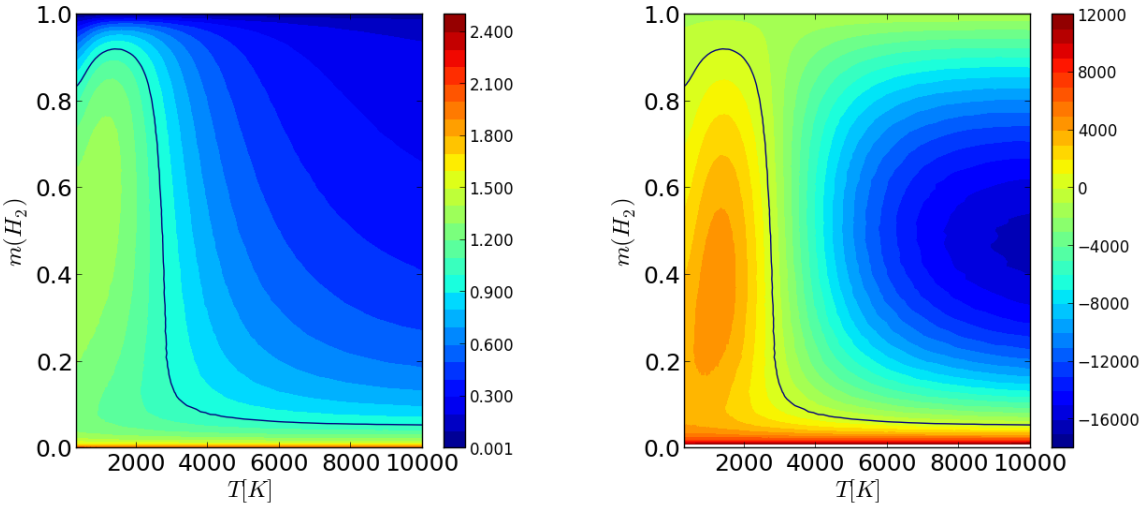
2. Convert the tetrafluoride mixture into a hexafluoride mixture using elemental fluorine as the fluorinating agent. Since AmF_4 does not fluorinate, the presence of solid AmF_4 particulates dispersed within the gaseous hexafluoride medium forms a colloidal system.

3. Mix the aerosol with molecular hydrogen (moderator) until the desired concentration is achieved.

Given the large variation in LWR SNF composition, let us focus on a particular scenario from the fuel cycle analysis group at the Idaho National Laboratory. [63, 64] The characteristics of this feedstock include: 4.21% initial enrichment; 50 GWd/t (gigawatt-days of thermal output per metric ton of heavy metal) burnup; 5 years of storage; and an additional 2 years of reprocessing and fabrication before reuse. Table 4 presents the renormalized transuranic isotopic mass fractions for a Pu-Only product stream and a Transuranic product stream.

Isotope	**Pu-Only**	**Transuranic**
^{237}Np	-	0.0679
^{238}Pu	0.0326	0.0290
^{239}Pu	0.5556	0.4944
^{240}Pu	0.2581	0.2297
^{241}Pu	0.0988	0.0879
^{242}Pu	0.0549	0.0489
^{241}Am	-	0.0280
^{242}Am	-	0.0002
^{243}Am	-	0.0140
k_∞	1.421	1.360
α [1/s]	3,320	2,670

Table 4: **Renormalized LWR SNF transuranic isotopic mass fractions. The MCNP5 k_∞ and α results correspond to a nanofuel with: $m(\mathbf{H}_2) = m(\mathbf{SNF}) = 0.5$, $\rho = 0.02$ g/cm^3, and $T = 879$ K.**



a) k_∞ **b)** α **[1/s]**

Figure 15: **10,100 MCNP5 simulations depicting (a)** k_∞ **and (b)** α **as a function of** $m(\mathbf{H_2}, \mathbf{Transuranic})$ **and** T **for a fixed** $\rho = 0.028$ **g/cm^3. The solid black contour corresponds to (a)** $k_\infty = 1$ **and (b)** $\alpha = 0$ **1/s.**

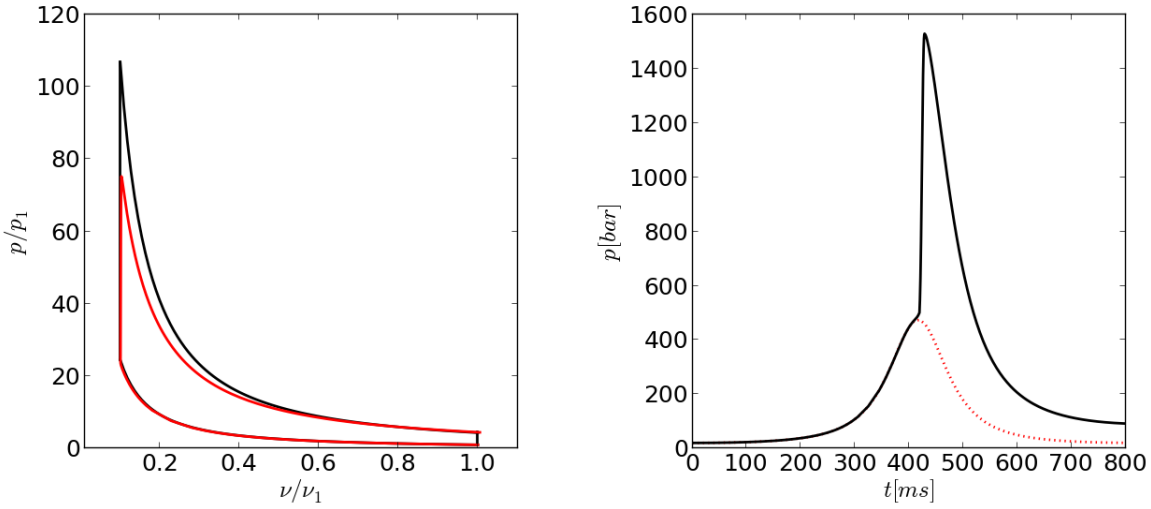
Table 4 includes MCNP5 k_∞ and α results for a nanofuel with: $m(\mathrm{H_2}) = m(\mathrm{SNF}) = 0.5$, $\rho = 0.02$ g/cm^3, and $T = 879$ K. SNF refers to either the Pu-Only or Transuranic isotopic distribution. For the Pu-Only (Transuranic) isotopic distribution $k_\infty = 1.421$ (1.360) and $\alpha = 3,320$ 1/s (2,670 1/s). The Transuranic nanofuel properties are comparable to Fuel d.

Figure 15 plots k_∞ and α as a function of the nanofuel ingredient mass fractions $m(\mathrm{H_2}, \mathrm{Transuranic})$ and T for a fixed $\rho = 0.028$ g/cm^3. The mass fractions form a convex combination and the mass fraction m(Transuranic) is found from $m(\mathrm{Transuranic}) = 1 - m(\mathrm{H_2})$. The abscissa (ordinate) reflects 100 (101) logarithmically (uniformly) spaced nanofuel temperatures (mass fraction m(Transuranic)).

Figure 15 illustrates a large range of supercritical ($k_\infty > 1$, $\alpha > 0$ 1/s) nanofuels at low T. In particular, there exists a sizeable plateau with $k_\infty \sim 1.3$ and $\alpha \sim 4,000$ 1/s. For moderator mass factions in the domain $0.2 < m(\mathrm{H_2}) < 0.8$, the nanofuels clearly exhibit a negative α_T with a criticality transition near $T \sim 2,700$ K.

Now let us model the performance of a 4-stroke reciprocating LWR SNF nanofuel engine operating in compression-ignition mode. Nanofuel engine simulation initialization includes:

1. Select the nanofuel with an equal mass fraction mixture of molecular hydrogen and the Transuranic isotopic distribution given in Table 4 ($m(\mathrm{H_2}) = m(\mathrm{Transuranic}) = 0.5$).



a) Otto cycle **b) p [bar]**

Figure 16: **Compression-ignition reciprocating LWR SNF nanofuel engine simulation. (a) Simulated (red) and ideal (black, $r = 10$, $\xi = 8.225$, and $\gamma = 1.389$) Otto cycle. (b) Nanofuel (black) and motored (dashed red) p as a function of time.**

2. Set the nanofuel properties in state 1: $\rho_1 = 0.0028$ g/cm^3 and $T_1 = 350$ K.
3. Assign the engine core dimensions: $R = H_1/20 = 60$ cm.
4. Use the piston moving boundary condition (see Eq. 23) with $l_r = 21.6$ m and $l_c = 5.4$ m, these dimensions form the optimal engine core geometry ($H = 2R$) when $r = 10$.
5. Surround the engine core with a 40 cm thick Be neutron reflector ($T = 800$ K).
6. Operate the engine at 0.6 cps and $S_N = 10^{14}$ N/s.

LWR SNF nanofuel engine simulation results include: $Q = 583.2$ MJ, $\xi = 8.225$, $T_3 = 2,723$ K, and $p_3 = 1,530$ bar. From App. B, the hoop stress (deflection) at the inner surface of the piston case is $\sigma_{\theta\theta} = 3,251$ bar ($u = 737.4\mu$m) and the Be yield strength is $\sigma_y(800K) = 2,114$ bar. Applying an external pressure of $p_{out} = 895.2$ bar to the piston case outer surface reduces the hoop stress at the inner surface of the piston case to 90% of the Be yield strength.

Figure 16a compares the simulated and ideal ($r = 10$, $\xi = 8.225$, and $\gamma = 1.389$) Otto cycles. In particular, the simulated (ideal) nanofuel engine efficiency is $\eta = 48.48\%$ (59.17%). LWR SNF nanofuel engine performance metrics include: net work per cycle $W = 282.7$ MJ; engine power $P = 169.6$ MW (2.274×10^5 hp); and electric power output $P_e = 166.2$ MW$_e$ (assuming

98% generator efficiency). Figure 16b illustrates the increase in nanofuel pressure during the combustion process compared to the motored pressure. The nanofuel pressure begins to depart from the motored pressure before the quarter cycle time ($t = 416.7$ ms) and peaks at $t = 428.6$ ms.

Compared to the compression-ignition nanofuel engine simulation in Sec 6.2, the compression-ignition LWR SNF nanofuel engine simulation releases less energy in a larger volume and operates at a lower speed. The decrease in engine core pressure improves the structural integrity. The decrease in operating speed is due to a decrease in the peak neutron population exponential growth factor from $\alpha \sim 425$ 1/s to $\alpha \sim 220$ 1/s. Since the electric power output is proportional to the operating speed, there is an equivalent reduction in electric power output from $P_e = 390.1$ MW_e to $P_e = 166.2$ MW_e.

These preliminary results demonstrate the feasibility of using the transuranic elements from LWR SNF in a nanofuel engine. The nanofuel can incorporate trace amounts of radioactive isotopes with minimal degradation in nanofuel engine performance. Compared to nanofuels comprised of the essential ingredients, the theft attractiveness of nanofuels comprised of the transuranic elements from LWR SNF decreases. [65]

8 Wankel nanofuel engine

The Wankel engine, named after the German engineer Felix H. Wankel, is a type of rotary engine. [66–68] It performs the intake, compression, expansion, and exhaust strokes while the engine core changes volume and the moving parts rotate in the same direction. For a power cycle the Wankel engine offers several advantages over the reciprocating engine, including:

1. an increase in the power system density, which is defined as the ratio of the engine core volume to the total engine volume;
2. a decrease in engine vibration, since the moving parts are in a continuous unidirectional motion and a rotating mass can be completely balanced by a counterweight;
3. the elimination of the intake-exhaust valve mechanism, which increases the engine operating speed and reduces the mechanical noise;
4. the elimination of the crank mechanism, which simplifies engine construction; and
5. a decrease in torque fluctuation, since the working fluid pressure is directly transmitted to the output shaft.

These advantages reduce cost.

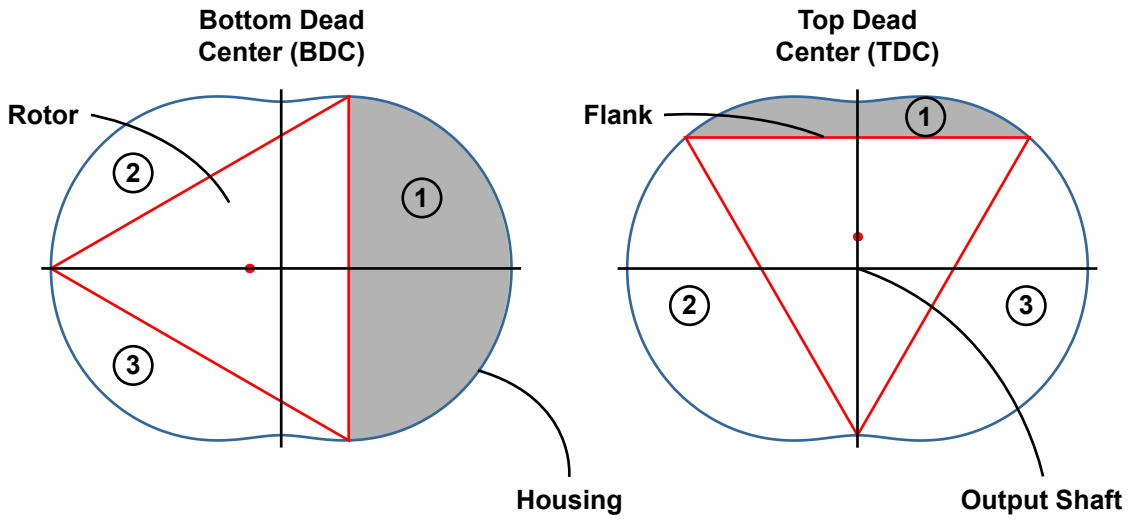


Figure 17: **Wankel engine working fluid volumes and the main Otto cycle engine core configurations, namely the bottom dead center (BDC) position (left) and the top dead center (TDC) position (right).**

This section reviews the Wankel engine geometry, adapts the Wankel engine to support a nuclear chain reaction, and explores compact and economical Wankel nanofuel engine configurations. The next section models Wankel nanofuel engine performance.

8.1 Wankel engine geometry

Figure 17 illustrates the Wankel engine two-lobe epitrochoid rotor housing and triangular rotor geometry. The rotor in a Wankel engine replaces the piston in a reciprocating engine. Instead of an oscillatory piston motion, the rotor executes a continuous unidirectional motion that directly transmits power to an output shaft.

The Wankel engine operates in an Otto cycle. During operation there are three variable working fluid volumes (engine cores) in different Otto cycle states. Each volume (V) contains a mass of fuel (M) that is constrained by the rotor housing, one rotor flank, and the side housing (which limits the volume along the output shaft axis). Figure 17 illustrates the three working fluid volumes along with the two main engine core configurations, namely the bottom dead center (BDC) position and the top dead center (TDC) position.

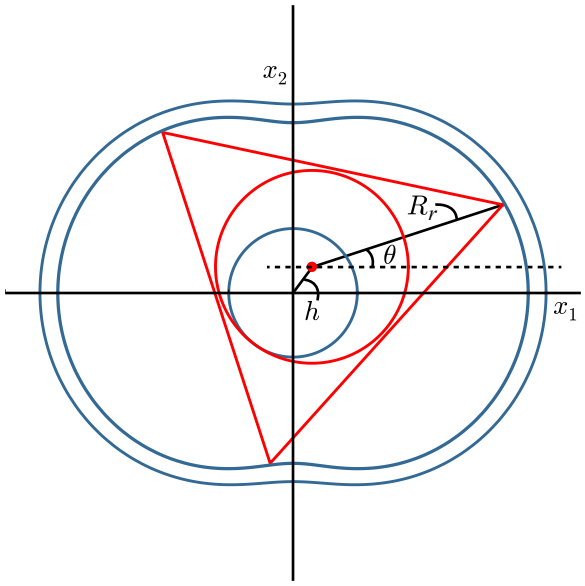


Figure 18: **Wankel engine rotor housing geometry.**

Figure 18 illustrates the Wankel engine rotor housing geometry. This two-lobe epitrochoid is given by

$$x_1(\theta) = R_r \cos(\theta) + h \cos(3\theta), \tag{24}$$

$$x_2(\theta) = R_r \sin(\theta) + h \sin(3\theta), \tag{25}$$

where (x_1, x_2) denotes the rotor housing curve in Cartesian coordinates, $\theta \in [0, 2\pi)$ is defined from the positive x_1-axis in the counterclockwise sense, R_r is the generating radius (rotor center-to-tip distance), and h is the eccentricity. [69] The rotor tip positions are given by

$$x_{1m}(\theta) = R_r \cos\left(\theta + \frac{2m\pi}{3}\right) + h \cos(3\theta), \tag{26}$$

$$x_{2m}(\theta) = R_r \sin\left(\theta + \frac{2m\pi}{3}\right) + h \sin(3\theta), \tag{27}$$

where $m \in [0, 1, 2]$.

The ratio of h to R_r is the eccentricity ratio (h/R_r), which is geometrically constrained to $h/R_r \in [0, 1/4)$. The upper limit requires a finite distance (d_1) between the rotor flank and the rotor housing minor axis when the engine core is in the TDC position:

$$d_1 = (R_r - h) - \left(\frac{1}{2}R_r + h\right) = \frac{1}{2}R_r - 2h > 0. \tag{28}$$

The lower limit delivers no compression $(r = 1)$ and generates no torque.

Flank rounding modifies the rotor flank to reduce the engine core volume in the TDC position. This increases the Wankel engine compression ratio and thermal efficiency. Figure 19

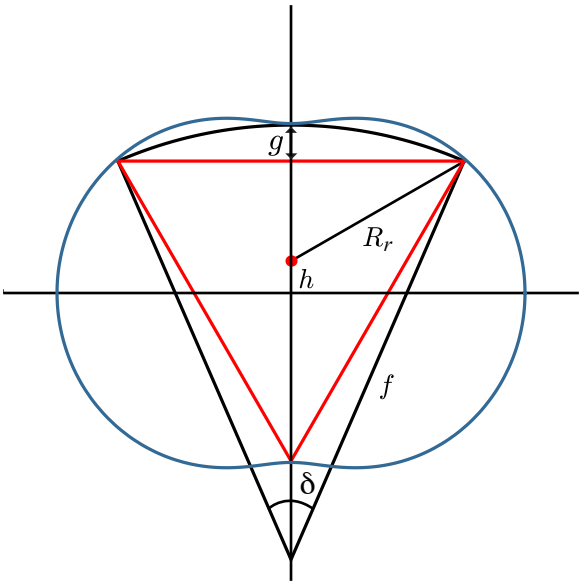


Figure 19: **Wankel engine circular arc flank rounding geometry.**

illustrates a circular arc flank, which is a common shape for flank rounding, and establishes the following geometric relations:

$$\frac{f}{R_r} = \frac{\sqrt{3}}{2} \csc\left(\frac{\delta}{2}\right), \tag{29}$$

$$\frac{g}{R_r} = \frac{\sqrt{3}}{2} \tan\left(\frac{\delta}{4}\right), \tag{30}$$

where f is the circular arc radius, δ is the angle subtended by the circular arc, and g is the maximum distance of the circular arc flank above the triangular flank. The condition $g < d_1$ ensures the rotor flank does not contact the rotor housing.

The Wankel engine compression ratio is given by

$$r = \frac{V_{max} - V_{seg}}{V_{min} - V_{seg}}, \tag{31}$$

where V_{max} (V_{min}) is the engine core volume in the BDC (TDC) position and V_{seg} is the additional rotor volume due to flank rounding. These volumes are given by

$$\frac{V_{max}}{R_r^2 w} = \pi \left[\left(\frac{h}{R_r}\right)^2 + \frac{1}{3}\right] + \frac{\sqrt{3}}{4}\left[6\left(\frac{h}{R_r}\right) - 1\right], \tag{32}$$

$$\frac{V_{min}}{R_r^2 w} = \pi \left[\left(\frac{h}{R_r}\right)^2 + \frac{1}{3}\right] - \frac{\sqrt{3}}{4}\left[6\left(\frac{h}{R_r}\right) + 1\right], \tag{33}$$

$$\frac{V_{seg}}{R_r^2 w} = \frac{3}{8}\frac{\delta - \sin(\delta)}{\sin^2(\delta/2)}, \tag{34}$$

where w is the rotor width.

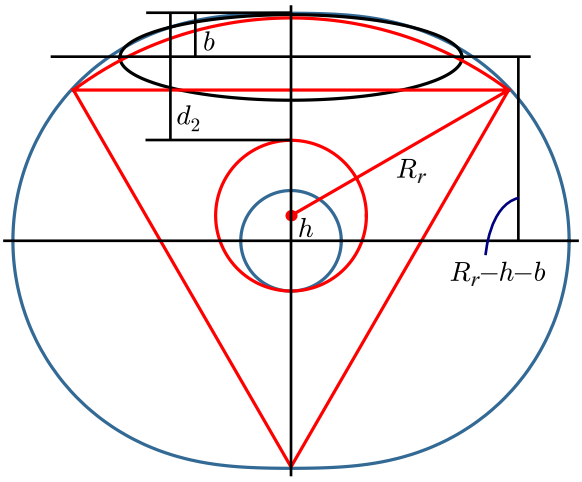


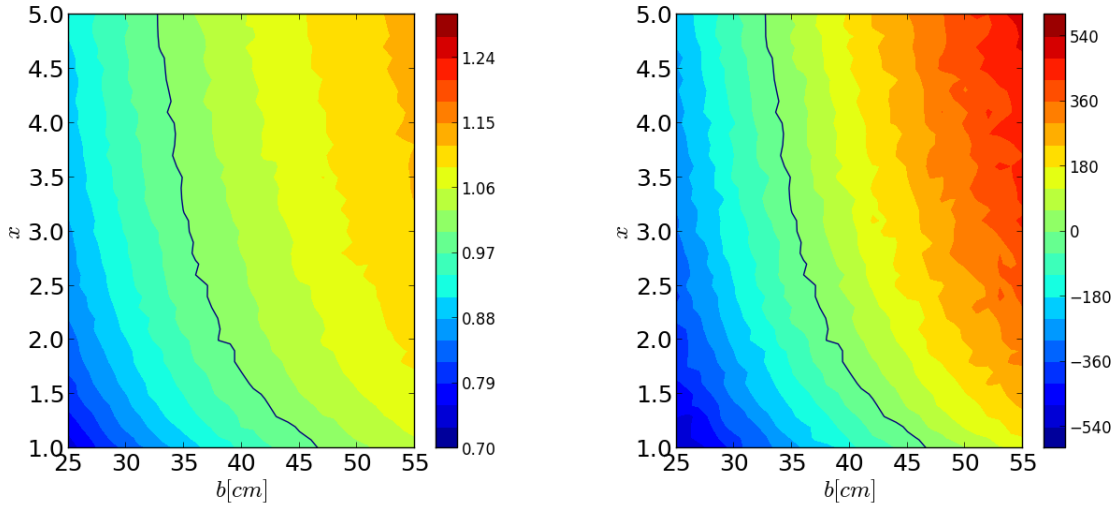
Figure 20: **Wankel nanofuel engine flank cavity geometry in the TDC position.**

8.2 Flank cavity design

Wankel engines introduce a flank cavity (or rotor recess) to improve performance. In an analogous fashion, let us study the behavior of a nanofuel (nuclear fuel) in a flank cavity (configuration designed to support a chain reaction).

A spherical geometry minimizes the surface-to-volume ratio and hence neutron leakage. Figure 17 shows that the engine core in the TDC position is elongated along the major axis. Ellipsoids naturally accommodate this elongated shape and maintain the favorable neutron leakage properties of a sphere. Figure 20 illustrates an ellipsoidal cavity with a minor axis length $2b$ and a major axis length $2a = 2xb$, where x is the ratio of the major axis length to the minor axis length and $x = 1$ corresponds to a sphere.

Figure 21 plots k_{eff} and α as a function of the ellipsoidal minor radius (b) and the multiplier x. The nanofuel is comprised of an equal mass fraction mixture of H_2 and the Transuranic isotopic distribution given in Table 4 ($m(H_2) = m(\text{Transuranic}) = 0.5$) at a fixed $\rho = 0.028$ g/cm^3 and $T = 734$ K. The engine core is surrounded by a 30 cm thick Be neutron reflector at $T = 573.15$ K (300 C). Figure 21 shows that the critical b decreases as x increases. In particular, the nanofuel is critical when: $b = 46.62$ cm, $x = 1.0$ (spherical cavity); $b = 36.00$ cm, $x = 2.734$; and $b = 32.70$ cm, $x = 5.0$. Comparing the $x = 1.0$ and $x = 5.0$ ($x = 2.734$) results, the volume increases by 72.53% (25.88%).



a) k_{eff} **b)** α **[1/s]**

Figure 21: **1,271 MCNP5 simulations depicting (a)** k_{eff} **and (b)** α **as a function of the ellipsoidal minor radius** (b) **and the multiplier** x**, where** $a = xb$**. The solid black contour corresponds to (a)** $k_{eff} = 1$ **and (b)** $\alpha = 0$ **1/s.**

8.3 Compact economical configurations

The Wankel nanofuel engine size and efficiency strongly affect cost. The size is a function of the generating radius (R_r), the eccentricity (h), the reflector thickness (Δ), and the ellipsoidal flank cavity dimensions $(b,\ a = xb)$. The thermal efficiency (η) is a function of the compression ratio (r). Let us consider how these quantities are related and search for configurations that minimize cost and maximize profitability.

Nuclear performance influences Δ and (b, a). Appendix A shows that there is a practical upper limit on the reflector thickness for a given material, which is $\Delta = 30$ cm for Be. Section 8.2 shows that there is a critical ellipsoidal size for a given type and mass of nanofuel. In general, selecting a nanofuel and performing theoretical or computational criticality calculations reveals a range of feasible flank cavity dimensions.

Mechanical performance influences several quantities. Figure 20 illustrates that the ellipsoidal flank cavity minor axis length and the reflector thickness $(2b + \Delta)$ must fit between the rotor housing and the output shaft rotor journal (d_2). For an output shaft rotor journal diameter of $6h$, this condition is

$$2b + \Delta = d_2 = R_r - 5h. \tag{35}$$

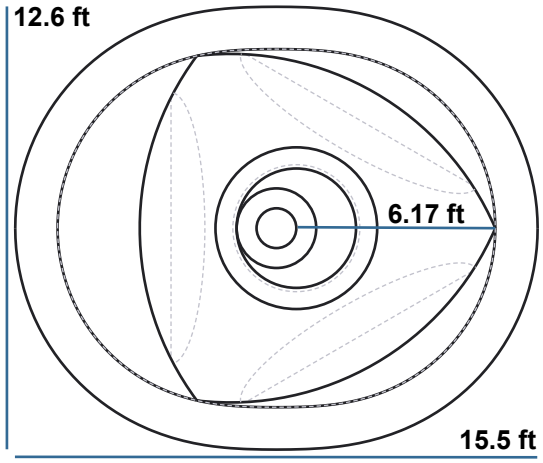


Figure 22: **Wankel nanofuel engine geometry.**

A generating radius solution to the above equation is

$$R_r = \frac{2b + \Delta}{1 - 5(h/R_r)} = \frac{2b + \Delta}{1 - 5(1/K)}, \tag{36}$$

where $K = R_r/h$ is the trochoid constant. Equation 36 shows that R_r decreases as K (h/R_r) increases (decreases), which is not obvious from the definition of K.

For $b = 32$ cm and $x = 4$, Eq. 36 reduces to

$$R_r[\text{cm}] = \frac{94}{1 - 5(1/K)}. \tag{37}$$

As K increases from 6 to 10, which is within the normal Wankel engine design space, R_r decreases from 564 cm to 188 cm. Figure 22 shows that for $K = 10$ the outer rotor housing major (minor) axis length is approximately 15.5 ft (12.6 ft).

Engine efficiency strongly influences profitability. To maximize efficiency and minimize the total engine volume, let us consider the quantity r/L_r, where $L_r = 2(R_r + h + \Delta)$ is the outer rotor housing major axis length. Using Eq. 36, setting the flank cavity major radius (a) to the intersection of the flank cavity major axis and the circular arc flank, and maximizing the quantity r/L_r gives the solution

$$K = 7.725 + 0.2105\Delta + 0.00013\Delta^2, \tag{38}$$

where Δ is in cm. This optimal condition is valid for any flank cavity minor radius (b).

These relationships among Wankel nanofuel engine quantities are merely a starting point. Although every application is different and every design will require a different optimization process, let us consider a generic Wankel nanofuel engine design that pulls together the results in this section:

1. Select the nanofuel comprised of an equal mass fraction mixture of H_2 and the Transuranic isotopic distribution given in Table 4 ($m(H_2) = m(\text{Transuranic}) = 0.5$).
2. Select a 30 cm thick Be reflector ($\Delta = 30$ cm).
3. Use Fig. 21 to select $b = 36$ cm.
4. Set a to the intersection of the flank cavity major axis and the circular arc flank, which is one of the assumptions used to derive Eq. 38.
5. Use Eq. 38 to find $K = 8.473$.
6. Use Eq. 36 to find $R_r = 248.9$ cm.

Other Wankel nanofuel engine properties include: $h = 29.37$ cm; $x = 4.420$ ($a = 159.1$ cm); $r = 4.735$ ($\eta = 45.39\%$); and the outer rotor housing major (minor) axis length is approximately 20.2 ft (16.0 ft).

Balancing nuclear and mechanical engine performance influences size, cost, and profitability. Although engine cost is generally proportional to size (and number of components), the same cannot be said of profitability. An incremental decrease in engine cost can produce a larger reduction in profitability. This is precisely what happened as LWRs (economies of scale) moved to SMRs (economies of mass manufacturing).

9 Advanced reactor performance

A nuclear reactor is an apparatus that sustains nuclear fission in a self-supporting chain reaction. [70] In the United States, the NRC has the mandate to regulate civil nuclear reactors and *ensure adequate protection of the environment and public health and safety and the common defense and security.* [71]

An advanced reactor is a nuclear reactor with, at a minimum, the same degree of protection of the environment and public health and safety and the common defense and security required for the current generation of operational commercial LWRs. In addition, *advanced reactors will provide enhanced margins of safety and/or use simplified, inherent, passive, or other innovative means to accomplish their safety and security functions.* [71]

This section models a Wankel nanofuel engine with a nanofuel comprised of the transuranic elements from LWR SNF. Since a Wankel nanofuel engine sustains nuclear fission in a self-supporting chain reaction, it is a nuclear reactor. Since a Wankel nanofuel engine has several advanced reactor attributes, such as the inherent safety features found in the nanofuel and dynamic engine core geometry, it is indeed an advanced reactor.

Wankel nanofuel engine simulation initialization includes:

1. Select the nanofuel comprised of an equal mass fraction mixture of H_2 and the Transuranic isotopic distribution given in Table 4 ($m(H_2) = m(\text{Transuranic}) = 0.5$).
2. Select a 30 cm thick Be neutron reflector ($T = 573.15$ K), which includes portions of the rotor and the rotor housing.
3. Assign $b = 36$ cm and set a to the intersection of the flank cavity major axis and the circular arc flank.
4. Set $K = 8.235$, which is slightly different from the optimal $K = 8.473$ given by Eq. 38 for $\Delta = 30$ cm. This modification increases the compression ratio. Now $R_r = 259.7$ cm, $h = 31.53$ cm, and $x = 4.568$.
5. Assign $w = 2(b + \Delta) = 132.0$ cm.
6. Select a 30 cm thick Cr-Fe-Ni alloy for the side housing ($T = 400$ K).
7. Set $\theta = -\pi/3$ at $t = 0$ s. This places the Wankel nanofuel engine in the BDC position identified in Fig. 17.
8. Set the engine core 1 nanofuel properties in state 1: $\rho_1 = 0.005670$ g/cm^3 and $T_1 = 400$ K. The other engine core properties are set by the engine core 1 performance.
9. Operate the Wankel nanofuel engine at 1/3 rotor rotations per second, where the engine has one power pulse per shaft rotation and three output shaft rotations per rotor rotation.
10. Operate the Wankel nanofuel engine in compression-ignition mode with an internal neutron source of $S_N = 10^{13}$ N/s.

Figure 23 illustrates the time evolution of the Wankel nanofuel engine simulation geometry, displaying snapshots at 250 ms time intervals. The compression stroke for engine core 1 (red) begins at $t = 0$ ms (BDC position) and ends at $t = 750$ ms (TDC position). Engine core 2 (blue) and engine core 3 (yellow) are phased 1,000 ms apart.

Wankel nanofuel engine simulation results include: $Q = 557.1$ MJ, $\xi = 6.504$, $T_3 = 2,525$ K, and $p_3 = 1,446$ bar. Figure 24a compares the simulated and ideal ($r = 4.939$, $\xi = 6.504$,

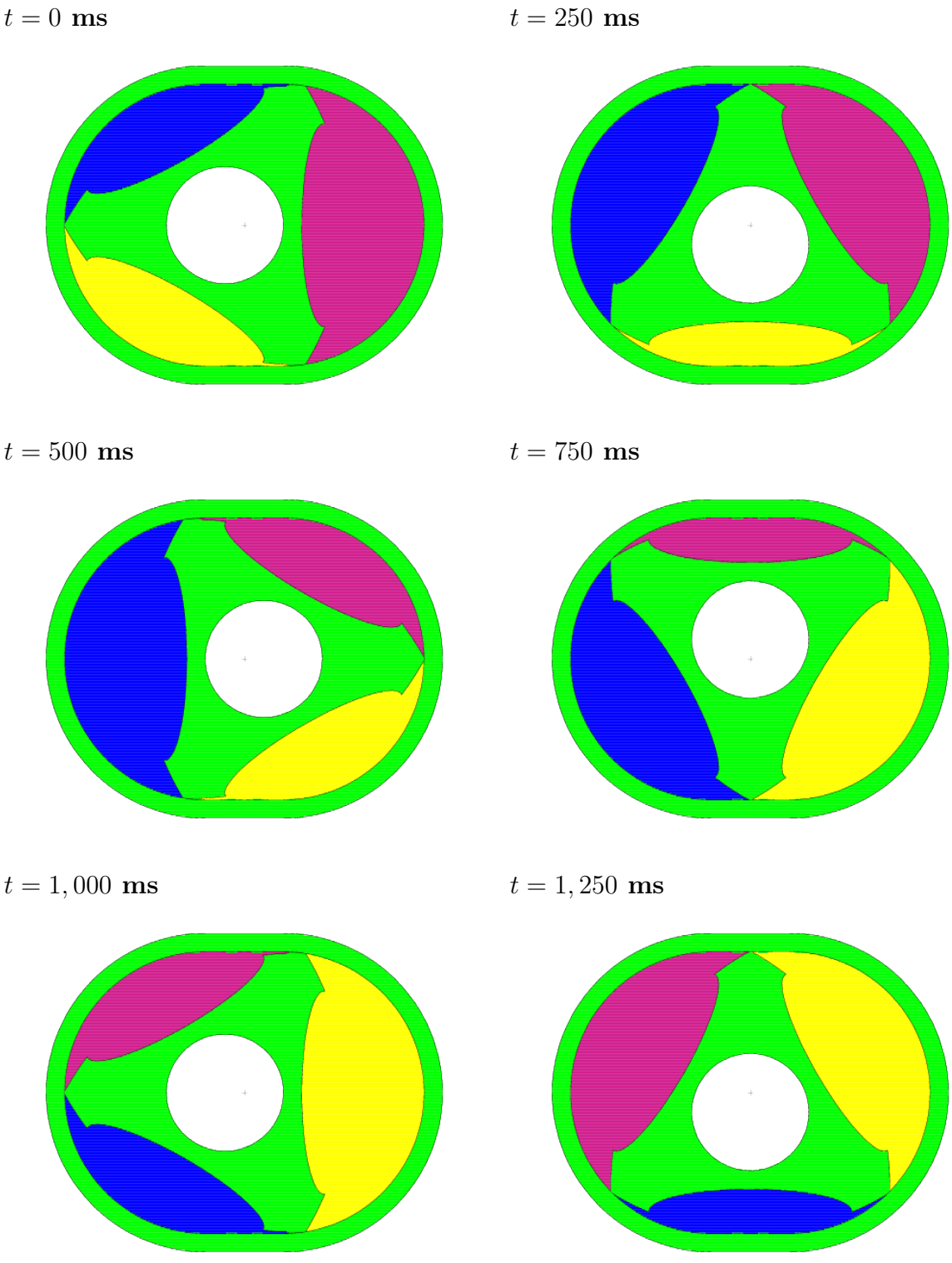
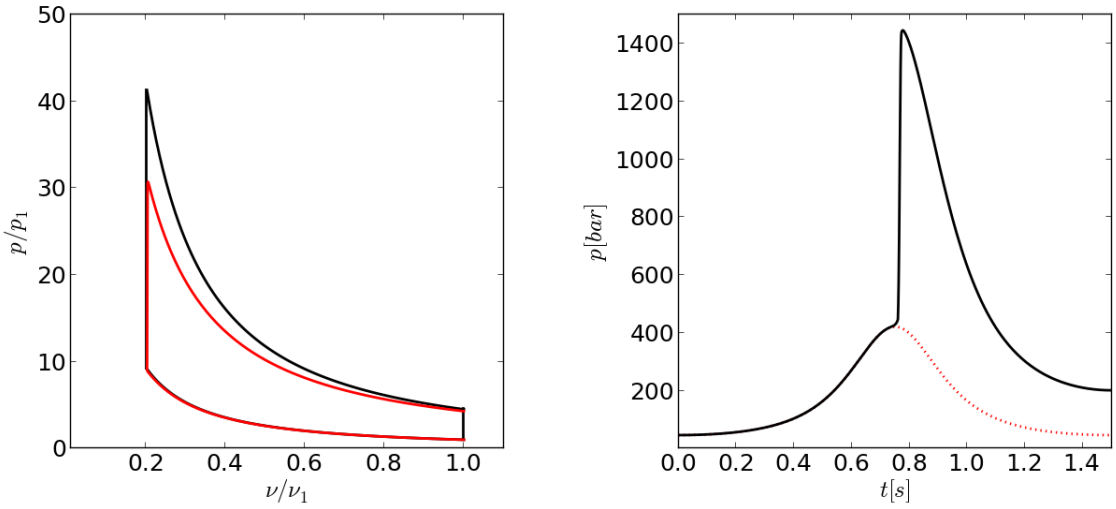


Figure 23: **Wankel nanofuel engine simulation geometry snapshots.**



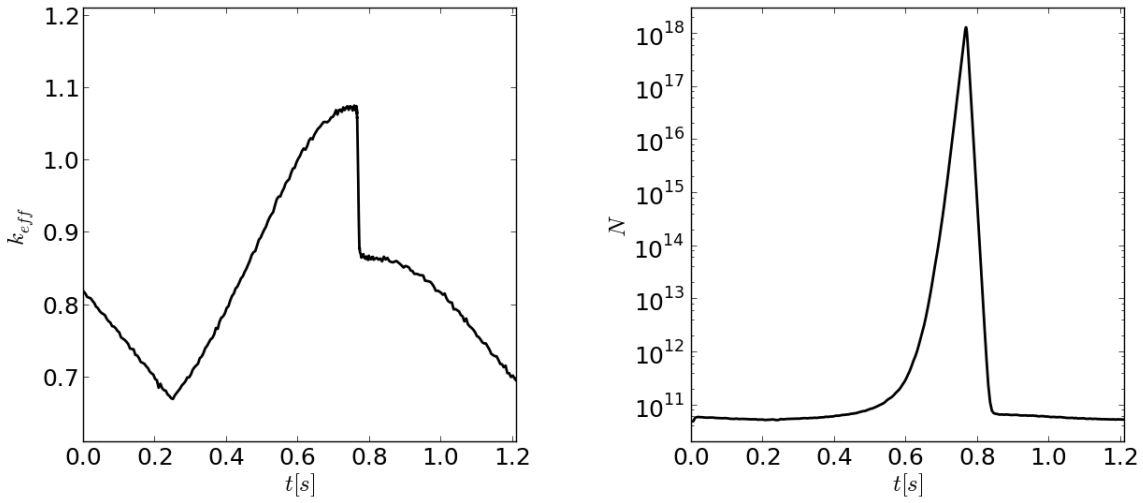
a) Otto cycle **b) p [bar]**

Figure 24: **Wankel nanofuel engine simulation. (a) Simulated (red) and ideal (black, $r = 4.939$, $\xi = 6.504$, and $\gamma = 1.387$) Otto cycle. (b) Nanofuel (black) and motored (dashed red) p as a function of time.**

and $\gamma = 1.387$) Otto cycles. In particular, the simulated (ideal) nanofuel engine efficiency is $\eta = 36.85\%$ (45.49%). Wankel nanofuel engine performance metrics include: net work per cycle $W = 205.3$ MJ; engine power $P = 205.3$ MW (2.753×10^5 hp); and electric power output $P_e = 201.2$ MW$_e$ (assuming 98% generator efficiency). Figure 24b illustrates the increase in nanofuel pressure during the combustion process compared to the motored pressure. The nanofuel pressure begins to depart from the motored pressure before the engine core reaches the TDC position ($t = 750.0$ ms) and peaks at $t = 776.3$ ms.

The structural integrity can be explored by examining the Be reflector surrounding the flank cavity when the engine core is in the TDC position. Taking a cross-section orthogonal to the flank cavity major axis and along the flank cavity minor axis, the engine core can be approximated as a thick-walled cylinder with radius $b = 36.0$ cm and thickness $\Delta = 30.0$ cm. From App. B, for $p_3 = 1,446$ bar the hoop stress (deflection) at the inner surface of the engine core is $\sigma_{\theta\theta} = 2,671$ bar ($u = 364.3\mu$m) and the Be yield strength is $\sigma_y(573.15\text{K}) = 2,884$ bar. This hoop stress is 92.61% of the Be yield strength.

Figure 25 plots two nuclear properties from the Wankel nanofuel engine simulation. Figure 25a (k_{eff}) shows that the system turns critical ($k_{eff} = 1$) at $t = 597.6$ ms ($\theta = 0.2044$). Early in time k_{eff} decreases as the nanofuel density in engine core 2 decreases; k_{eff} begins to increase during the engine core 1 compression stroke; k_{eff} rapidly drops during the com-



a) k_{eff} **b)** N

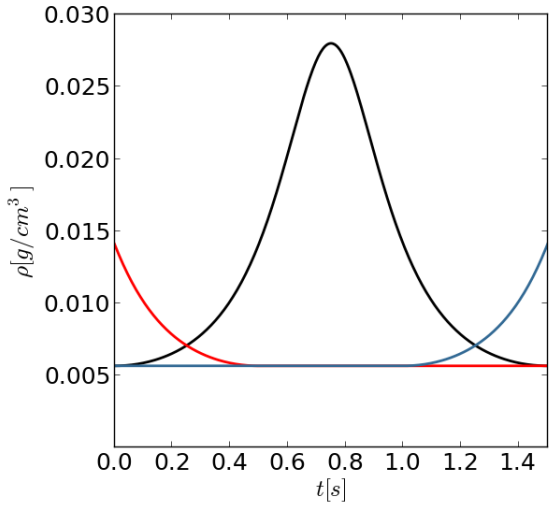
Figure 25: **Wankel nanofuel engine simulation depicting (a) k_{eff} and (b) N as a function of time.**

bustion process due to the nanofuel negative α_T; and then k_{eff} decreases during the engine core 1 expansion stroke.

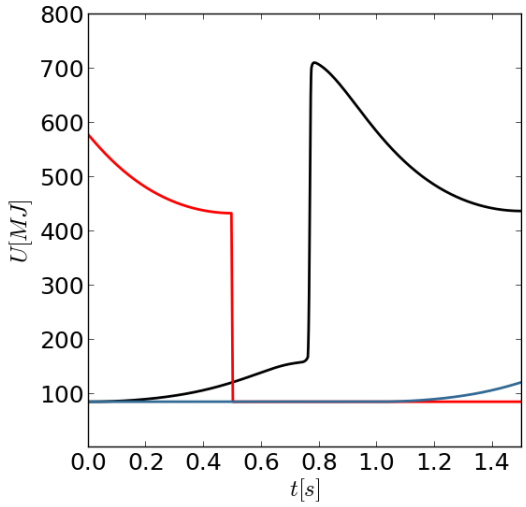
Figure 25b (N) shows that the neutron population does not exponentially amplify until the system turns critical. The neutron population peaks at $t = 766.9$ ms, which is 169.3 ms after the system turns critical. It also shows that the neutron population rapidly decreases to the background level within 60 ms after the peak time. The Wankel nanofuel engine simulation combustion process lasts approximately 230 ms and the Nordheim-Fuchs burst duration is approximately $\tau_b = 29$ ms. Thus, the combustion process significantly overlaps the compression and expansion strokes.

The Wankel nanofuel engine is inherently safe. It only releases nuclear energy after successful intake and compression strokes. The combustion process is limited by either the nanofuel negative α_T or, at higher operating speeds, the increase in engine core volume during the expansion stroke.

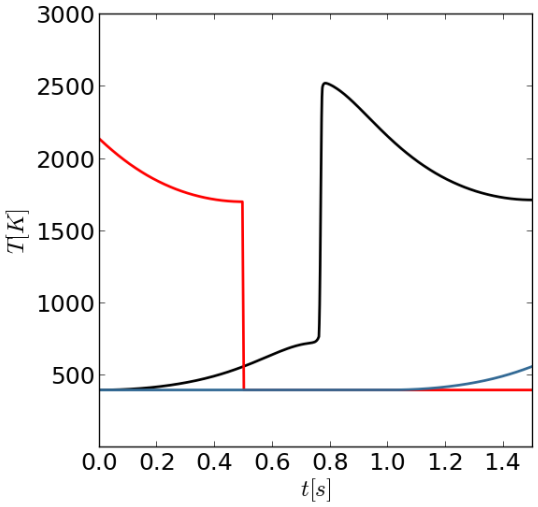
Figure 26 plots several nanofuel properties as a function of time from the Wankel nanofuel engine simulation. During the exhaust and intake process (process 4-1) the simulation maintains the nanofuel in state 1. Figure 26a plots ρ for the three engine cores. Engine core 1 performs a compression (expansion) stroke from $t = 0$ ms ($t = 750$ ms) to $t = 750$ ms ($t = 1,500$ ms); engine core 2 ends an expansion stroke at $t = 500$ ms; and engine core 3 begins a compression stroke at $t = 1,000$ ms.



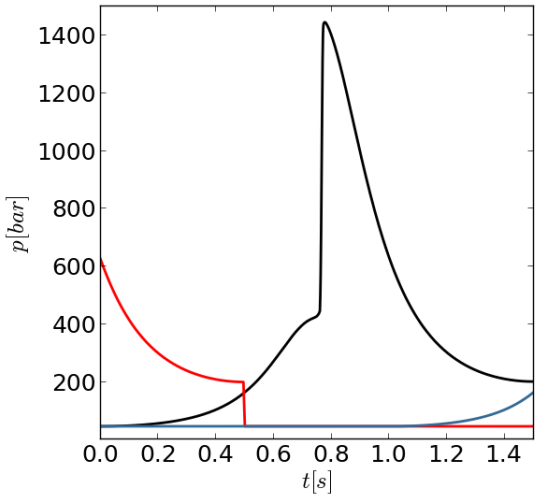
a) ρ **[g/cm^3]**



b) U **[MJ]**



c) T **[K]**



d) p **[bar]**

Figure 26: **Wankel nanofuel engine simulation depicting several nanofuel properties as a function of time. Engine core 1 (2) [3] is black (red) [blue].**

Figure 26b shows that the exhaust heat in the Wankel nanofuel engine is $Q_{41} = -351.8$ MJ. This heat can be converted into useful work using turbines in either a turbocharged (see Fig. 5) or turbocompounding (see Fig. 6) configuration. A 60% thermal-to-electric conversion efficiency provides an additional electric power output $P_e = 211.1$ MW_e.

Each engine core in the Wankel nanofuel engine simulation contains $N_0 = 1.683 \times 10^{25}$ fissile fuel ($^{239}PuF_6$) molecules and each power cycle produces $N_f = 2.189 \times 10^{19}$ fissions, assuming the effective energy released per ^{239}Pu fission is 198.5 MeV/f and 80% of this energy is deposited in the nanofuel [16]. Therefore, the initial mass of nanofuel (M) in an engine core contains fissile fuel for 7.701×10^5 power cycles assuming complete fuel utilization.

A Wankel nanofuel engine power plant, with $40M$ of nanofuel loaded into the fuel system and operated at 1/3 rotor rotations per second, can operate continuously for 320.9 days before the fissile fuel reaches 90% burnup. The operating duration is proportional to the operating speed. Upon initial nanofuel loading the fuel system contains $40m(^{239}PuF_6) = 394.8$ kg (870.4 lbs) of fissile fuel, where the fissile fuel mass in an engine core is $m(^{239}PuF_6) = 9.869$ kg, and $40m$(Transuranic) = 798.5 kg (1,760 lbs) of nuclear material. Compared to an AP1000 pressurized-water reactor (PWR), the Wankel nanofuel engine (advanced reactor) power plant contains approximately 120 times less nuclear material. [36]

The Wankel nanofuel engine fulfills two **obvious safety** criteria, identified by Dr. Edward Teller, that are important for the widespread public acceptance of an advanced reactor design. [72]. First, the entire power plant can be placed underground and heavily fortified against natural disasters and sabotage. Andrei D. Sakharov advocated this design measure. The Wankel nanofuel engine cross section (21.1 ft × 16.6 ft) is comparable to a 200 MW_e-class electric generator (12.1 ft × 22.3 ft) and the entire power system is less than 60 ft long. Second, the Wankel nanofuel engine functions autonomously and is shielded from all types of human error. The engine operating speed and orificing strongly affect the electric power output and permit rapid load following. Similar to a backup generator, the Wankel nanofuel engine can automatically start and stop as needed.

10 Outlook

Economics determines the market adoption of power generation technology. To a lesser extent, the safety and waste management facets of the power generation technology may influence market penetration. For any nuclear technology there is the added concern of nuclear weapon proliferation. This section analyzes the economic, safety, waste management, and nonproliferation attributes of a Wankel nanofuel internal engine electric power plant and

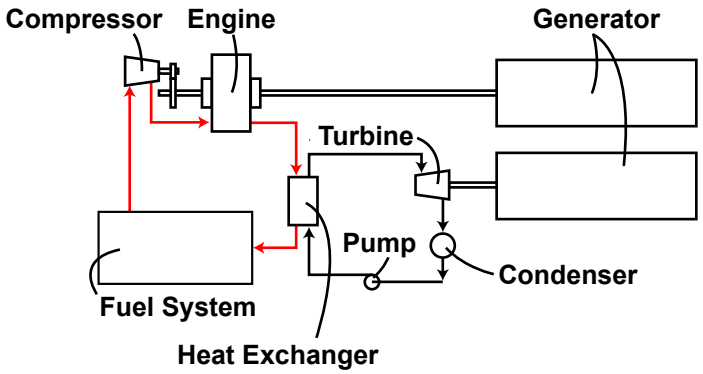


Figure 27: **Schematic 420 MW$_e$ Wankel nanofuel engine electric power plant.**

concludes with a brief statement on the enormous positive impact this revolutionary new power generation technology can have on the quality of life for present and future generations around the world.

Let us begin by considering an electric power plant comprised of a Wankel nanofuel engine in a mechanical supercharging configuration. Figure 27 illustrates a power plant configuration for the Wankel nanofuel engine presented Sec. 9. This is a 420 MW$_e$ power plant containing two 234 megavolt-ampere (MVA), 13.8 kilovolt (kV), 60 hertz (Hz) electric generators.

The Wankel nanofuel engine is sized to maximize the compression ratio and minimize the overall engine volume. Although moving to a higher compression ratio increases the thermal efficiency and allows more direct power from the engine, the added cost diminishes the benefit. At this size the exhaust contains a significant amount of energy. To balance the electric power produced by the engine and the exhaust, Sec. 9 set $K = 8.235$ over the optimal $K = 8.473$. A different balance between producing useful work and generating heat can be selected for different applications. In general, nanofuel engine power plant configurations can easily be developed to meet rapidly changing (over the course of seconds) electric power and heat demands.

10.1 Economics

Let us start this power plant economic analysis with an estimate of the overnight capital cost (OCC). This estimate follows the methodology established by the US Energy Information Administration (EIA) to compare the OCC of different power plant technologies. [73, 74]

The Wankel nanofuel engine electric power plant OCC is divided into several capital cost categories, including:

Civil and structural material and installation costs include site preparation activities, such as: clearing trees; constructing roads; installing drainage and underground utilities; pouring concrete foundations; installing structural steel; and constructing buildings. Compared to other power plants, an additional cost allowance is made for underground installation. This provides fortification and physical protection from natural disasters and sabotage.

Mechanical equipment supply and installation costs include power system equipment, such as: the nanofuel engine; the fuel system; auxiliary equipment (compressor, heat exchanger, pump, condenser); steam turbine; and balance of plant equipment. There is economic uncertainty in the nanofuel engine and the fuel system cost estimates. A recent Electric Power Research Institute report on power generation technology found that the unit cost prior to commercialization is typically a factor of 2-3 larger than predicted during the ideation stage. [75] Therefore, nanofuel engine power plant implementation plans account for a three-fold cost escalation before commercialization.

Electrical instrumentation and control supply and installation costs include electrical commodities, such as: electric transformers; switchgear; motor control centers; switchyard; distributed control systems and instrumentation; and electrical commodities. Each generator is connected to a high-voltage bus in the switchyard by a dedicated generator circuit breaker (GSU) and a disconnect switch. The GSU is designed to step-up the generator voltage to the transmission voltage.

Project indirect and contingency costs are expenses that do not directly fit into a specific capital cost category and account for unforeseen events or circumstances.

Engineering, procurement, and construction (EPC) cost is the sum of the mechanical equipment supply and installation, electrical instrumentation and control supply and installation, electrical instrumentation and control supply and installation, and project indirect and contingency costs.

Owner costs include preliminary feasibility and engineering studies, environmental studies, licensing, legal services, insurance, property taxes prior to operation, and electrical interconnect equipment. There is economic uncertainty in this cost estimate, which leverages early US Department of Energy (DOE) reports that included DOE-industry cost sharing scenarios for licensing new nuclear power plants. [76, 77] and uses information from a more recent DOE report discussing the lessons learned by electric utilities in obtaining an ESP. [78].

Table 5 summarizes the Wankel nanofuel engine electric power plant OCC estimate. The OCC is 170.0 million 2015$ (2015 US dollars) for a 420 MW_e power plant or 404.8 2015$/$kW_e$. Table 6 shows that this OCC is more economical than any fossil fuel power plant on the market; Table 7 shows that this OCC is an order-of-magnitude better than alternative energy power generation technology. For an electric power generating station comprised of several nanofuel engine power plants the owner cost for subsequent plants is negligible. Thus, to build a second plant the OCC is close to the EPC cost, which is 125.0 million 2015$ for a 420 MW_e power plant or 297.6 2015$/$kW_e$.

Now let us consider the financing cost, operation and maintenance cost, and fuel cost. The financing cost is dominated by the cost of capital, which is commensurate with an entities business and financial risk, and the project duration, which is significantly reduced by the economies of mass manufacturing.

The operation and maintenance cost can be estimated from recent EIA data on the average power plant operating expenses of major US-investor-owned electric utilities. [79] The average operation cost for gas turbine and small scale power plants in 2012 was 2.46 2012$ per megawatt-hour (2012$/MWh); the average maintenance cost for gas turbine and small scale power plants in 2012 was 2.76 2012$/MWh. The nanofuel engine plant will have additional security requirements imposed by the NRC that give rise to an extra operating cost of 5.43 2015$/MWh. Although these numbers can be improved by an order-of-magnitude, they can serve as a starting point for future economic discussions.

In 2014 the Henry Hub natural gas spot price averaged 35.8 2014$/MWh. [80] In April 2015 the Powder River Basin coal spot price was 6.00 2015$/MWh. [81] This factor-of-six price difference, where natural gas costs significantly more than coal, balances the factor-of-three difference in OCC and operation and maintenance cost, where coal power plants cost significantly more to build and operate than natural gas power plants. The result sets the market price for electricity generation.

For the nanofuel engine power plant the targeted fuel cost is 0.0 2015$/MWh. A negative (positive) fuel cost implies a profit on the consumption of LWR SNF. Since energy consumption is proportional to economic output, and the standard of living, both negative and positive fuel costs are counterproductive. A negative fuel cost requires taxpayers to indirectly pay more for energy; a positive fuel cost directly increases the price of energy by slowing market penetration.

Capital cost category	Million 2015$
Civil and structural material and installation	15.0
Mechanical equipment supply and installation	55.0
Electrical instrumentation and control supply and installation	30.0
Project indirect and contingency	25.0
Engineering, procurement, and construction (EPC)	**125.0**
Owner	45.0
Overnight capital cost (OCC)	**170.0**

Table 5: **Wankel nanofuel engine electric power plant OCC estimate.**

Power Plant	Capacity [kW_e]	OCC [$/$kW_e$]	OCC [$M]
Coal			
Single Unit Advanced PC	650,000	3,246	2,110
Dual Unit Advanced PC	1,300,000	2,934	3,814
Single Unit Advanced PC with CCS	650,000	5,227	3,398
Dual Unit Advanced PC with CCS	1,300,000	4,724	6,141
Single Unit IGCC	600,000	4,400	2,640
Dual Unit IGCC	1,200,000	3,784	4,541
Single Unit IGCC with CCS	520,000	6,599	3,431
Natural Gas			
Conventional CC	620,000	917	569
Advanced CC	400,000	1,023	409
Advanced CC with CSS	340,000	2,095	712
Conventional Combustion Turbine	85,000	973	83
Advanced Combustion Turbine	210,000	676	142
Fuel Cells	10,000	7,108	71

Table 6: **Fossil fuel electric power plant OCC estimates. [74] Capacity is in units of kW_e and the OCC is in units of 2012$/$kW_e$ or million 2012$ ($M). Abbreviations include: carbon capture and sequestration (CCS); combined cycle (CC); integrated gasification combined cycle (IGCC); and pulverized coal (PC).**

Power Plant	Capacity [kW_e]	OCC [$/$kW_e$]	OCC [$M]
Nuclear, Nanofuel Engine	420,000	405	170
Nuclear, Dual Unit	2,234,000	5,530	12,354
Hydroelectric	500,000	2,936	1,468
Hydro, Pumped Storage	250,000	5,288	1,322
Wind, Onshore	100,000	2,213	221
Wind, Offshore	400,000	6,230	2,492
Solar, Thermal	100,000	5,067	507
Solar, Small Photovoltaic	20,000	4,183	84
Solar, Large Photovoltaic	150,000	3,873	581
Geothermal, Dual Flash	50,000	6,243	312
Geothermal, Binary	50,000	4,362	218
Biomass, Combined Cycle	20,000	8,180	164
Biomass, Bubbling Fluidized Bed	50,000	4,114	206
Municipal Solid Waste	50,000	8,312	416

Table 7: **Alternative energy electric power plant OCC estimates. [74] Capacity is in units of kW_e and the OCC is in units of 2012$/$kW_e$ or million 2012$ ($M).**

10.2 Safety

The Wankel nanofuel engine has two important inherent safety features. First, the nanofuel has a negative α_T. As the nanofuel temperature increases, k decreases and the system turns subcritical. Second, the dynamic engine core geometry decreases the system criticality as the engine core moves away from the TDC position. When the engine core volume increases, ρ decreases and the neutron leakage increases.

There are additional safety features in the fuel system. With $40M$ of nanofuel loaded into the fuel system, the engine can operate for 320.9 days and contains approximately 100 times less nuclear material than commercial LWRs. This greatly reduces the source term in an accident scenario. The fuel system also avoids the LWR decay heat problem. Decay heat is due to radioactive decay in the nuclear fuel. In an accident scenario, LWR coolant and power to circulate the coolant are required to remove the decay heat and maintain the solid fuel in the reactor core at temperatures below the melting temperature. In the nanofuel engine fuel system no coolant or external power is required to manage the decay heat. The fission products are removed as part of the continuous recycling fuel system.

Finally, the Wankel nanofuel engine has two important obvious safety features, which are important for public acceptance. First, the entire power plant can be placed underground and heavily fortified against natural disasters and sabotage. Second, the engine functions autonomously and is shielded from all types of human error.

10.3 Waste management

The Wankel nanofuel engine electric power plant has no greenhouse gas emissions and operates in a closed thermodynamic cycle that permits complete fuel utilization. Scheduling mechanical equipment minor (major) maintenance every 8,000 (24,000) hours of operation provides a regular opportunity to add nanofuel and remove fission products.

Fuel efficiency can be improved by introducing fertile fuel into the nanofuel. In particular, for the nanofuel comprised of the transuranic elements from LWR SNF, introducing uranium isotope 238 hexafluoride ($^{238}UF_6$) provides a modest breeding ratio.

The Blue Ribbon Commission (BRC) on America's Nuclear Future was chartered to recommend a new strategy for managing the back end of the nuclear fuel cycle. In 2012 the BRC issued a final report that details important failings in the present nuclear fuel cycle, recommends the creation of a new nuclear waste management organization, and announces the large cost to the taxpayers incurred by implementing a deeply flawed nuclear waste management program. [82]

By consuming the transuranic elements from LWR SNF, which contains the long-lived radioactive material from past, present, and future commercial nuclear power plants, the nanofuel power plant eliminates the need for long-term, high-cost, and very unpopular geological nuclear waste repositories. The nanofuel engine can help reshape the back end of the nuclear fuel cycle, reduce the present economic and environmental nuclear waste burden on society, and stimulate nuclear power growth during the second nuclear era.

10.4 Nonproliferation

Commercial nuclear reactors operating today are almost exclusively of the LWR-type developed for producing plutonium during World War II. For electric power generation these early reactors were modified by: replacing the graphite moderator with water for use in a Rankine cycle; increasing the isotopic concentration of fissile fuel in natural uranium; and introducing inherent safety features, such as a negative α_T. [72]

Plutonium-uranium reduction extraction (PUREX) was also developed during World War II to separate plutonium from LWR SNF. During the first nuclear era, PUREX was an integral part of reprocessing commercial LWR SNF and the back-end of the nuclear fuel cycle. For example, from 1966-1972 the Western New York Nuclear Service Center used PUREX to process 640 metric tons of LWR SNF. [83]

Today there is an ongoing concern that the dissemination of LWR and PUREX technology will encourage nuclear weapon proliferation. History is full of examples where this has already occurred. [84]

In 1976, shortly after India detonated a nuclear device, President Gerald R. Ford announced

> *the reprocessing and recycling of plutonium should not proceed unless there is sound reason to conclude that the world community can effectively overcome the associated risks of proliferation . . . that the United States should no longer regard reprocessing of used nuclear fuel to produce plutonium as a necessary and inevitable step in the nuclear fuel cycle, and that we should pursue reprocessing and recycling in the future only if they are found to be consistent with our international objectives. [85]*

When President Ford issued this statement there was a confident belief that scientists would develop proliferation resistant nuclear power solutions within five years. This did not happen, and in 1981 President Ronald W. Reagan announced the *lifting [of] the indefinite ban which previous administrations placed on commercial reprocessing activities in the United States.* [85]

In sharp contrast to the nuclear technology developed during World War II for defense applications, the nanofuel engine consumes plutonium and the nanofuel can be created without separating plutonium into a separate product stream. In addition, enrichment facilities are not required to create nanofuel.

For any nuclear technology the potential threat from a **dirty bomb** is also a concern. Charles G. Bathe *et al.* [65] defines a potential nuclear threat as *the point at which the nuclear explosive energy exceeds the conventional explosive enegy.* Dirty bombs release less nuclear explosive energy than the conventional explosive energy and distribute radioactive material over a larger area. The nanofuel engine consumes the transuranic elements from LWR SNF and decreases the possible inventory of radioactive material that could be used in dirty bomb.

10.5 Summary

Nanofuel internal engine power plants have favorable economic, safety, and waste management attributes when compared to existing power generation technology. An economic advantage is sufficient to ensure market adoption. Safety and waste management improvements provide environmental benefits and facilitate public acceptance. Nonproliferation characteristics are necessary for global market penetration.

The Industrial Revolution increased the quality of life for many and moved Europe out of the Dark Ages. Today, 750 million people are without access to clean drinking water and more than 840,000 people die each year from water related diseases. [86] Access to affordable energy is the solution. The nanofuel internal engine offers an affordable clean energy solution for the 21^{st} century and can improve the quality of life for present and future generations around the world. With favorable economics the second nuclear era drive a second Industrial Revolution.

A Housing neutron transport

Neutron reflectors reduce the neutron leakage from the engine core. Facilitating the selection of a suitable nanofuel engine neutron reflector, this appendix analytically determines the probability that a fission neutron is thermalized in the reflector and returned to the engine core. This analytic approach closely follows the work of George I. Bell [87] and incorporates established nuclear data [16, 39].

Let us begin by considering a nanofuel bracketed by two semi-infinite reflectors in slab geometry. In the analysis:

1. assume the fast neutrons escape the nanofuel and enter the reflector;
2. employ Fermi age theory to describe the deceleration of neutrons from fast to thermal energies in the reflector; and
3. use a one-speed diffusion model to calculate the subsequent migration of thermal neutrons from the reflector to the nanofuel.

From Fermi age theory, the slowing down density S for a plane source of one fission neutron per second in an infinite non-absorbing medium is

$$S(z, \tau_F) = \frac{1}{\sqrt{4\pi\tau_F}} \exp\left\{\frac{-z^2}{4\tau_F}\right\}, \tag{39}$$

where z is the distance from the nanofuel-reflector interface and τ_F is the Fermi age. The slowing down density at the age to thermal is the source of thermal neutrons. Next, the transport of thermal neutrons is governed by the one-speed one-dimensional neutron diffusion equation:

$$\frac{d^2\phi}{dz^2} - \frac{1}{L^2}\phi = \frac{-S}{D}, \tag{40}$$

where ϕ is the neutron flux and the other quantities are defined in Sec. 4.

Equation 40 is solved using the Green function (kernel) method. The kernel function is

$$\phi(z) = \frac{1}{2\kappa D}\int_{-\infty}^{\infty} S(y)e^{-\kappa|z-y|}dy, \tag{41}$$

where $\kappa = 1/L$. Inserting Eq. 39 (source function) into Eq. 41 (kernel function) and integrating gives the following neutron flux solution:

$$\phi(z) = Ae^{-\kappa z} + \frac{e^{\tau_F\kappa^2}}{4\kappa D}\left\{2\cosh(\kappa z) + e^{-\kappa z}\Phi(\beta_-) - e^{\kappa z}\Phi(\beta_+)\right\}, \tag{42}$$

where

$$\beta_\pm = \frac{z}{2\sqrt{\tau_F}} \pm \kappa\sqrt{\tau_F} \tag{43}$$

and Φ is the error function

$$\Phi(z) = \frac{2}{\sqrt{\pi}}\int_0^z e^{-t^2}dt. \tag{44}$$

The unknown constant A is found from the boundary condition $\phi(0) = 0$. The result is

$$A = -\frac{e^{\tau_F\kappa^2}}{2\kappa D}\left[1 - \Phi(\sqrt{\tau_F}\kappa)\right]. \tag{45}$$

Collecting terms, the neutron flux is given by

$$\phi(z) = -\frac{e^{\tau_F\kappa^2}}{2\kappa D}\left[1 - \Phi(\sqrt{\tau_F}\kappa)\right]e^{-\kappa z} + \frac{e^{\tau_F\kappa^2}}{4\kappa D}\left\{2\cosh(\kappa z) + e^{-\kappa z}\Phi(\beta_-) - e^{\kappa z}\Phi(\beta_+)\right\}. \tag{46}$$

The current into the nanofuel is found from Fick's law applied to the nanofuel-reflector interface:

$$D\frac{d\phi}{dz}\bigg|_{z=0} = \frac{1}{2}e^{\tau_F\kappa^2}\left[1 - \Phi(\sqrt{\tau_F}\kappa)\right]. \tag{47}$$

Since there are two reflectors, Eq. 47 is half the probability that a fission neutron is thermalized in either reflector and returned to the nanofuel. Thus, the total probability P_∞ is

$$P_\infty(\tau_F, L) = e^{\tau_F\kappa^2}\left[1 - \Phi(\sqrt{\tau_F}\kappa)\right], \tag{48}$$

which is only a function of the dimensionless parameter $\sqrt{\tau_F}\kappa = \sqrt{\tau_F}/L$. This dimensionless parameter is the ratio of the distance traveled while slowing down to the distance traveled following thermalization and should be much less than one for a good reflector.

Now let us consider a nanofuel bracketed by two finite thickness reflectors in slab geometry. Assuming the slowing down density S has no slope at the fuel-reflector interface ($z = 0$) and vanishes at the external reflector boundary ($z = \Delta$), Bell [87] found the following solution to the age equation:

$$S(z,\tau_F,\Delta) = \frac{1}{\sqrt{4\pi\tau_F}}\left[\exp\left\{\frac{-z^2}{4\tau_F}\right\} - \frac{\exp\left\{\frac{-(z-2\Delta)^2}{4\tau_F}\right\} + \exp\left\{\frac{-(z+2\Delta)^2}{4\tau_F}\right\}}{1+\exp\left\{\frac{-2\Delta^2}{\tau_F}\right\}}\right]$$
$$= \frac{\exp\left\{\frac{-z^2}{4\tau_F}\right\}}{\sqrt{4\pi\tau_F}}\left[1-\cosh\left(\frac{\Delta z}{\tau_F}\right)\operatorname{sech}\left(\frac{\Delta^2}{\tau_F}\right)\right]. \tag{49}$$

Similar to the semi-infinite reflector case, insert Eq. 49 (source function) into Eq. 41 (kernel function), carry out the integration, apply Fick's law, and account for both reflectors to find the total probability P_Δ that a fission neutron is thermalized in either reflector of finite thickness Δ and returned to the nanofuel. The solution is

$$\begin{aligned} P_\Delta(\tau_F,L,\Delta) =& e^{\tau_F\kappa^2}\left\{\Phi(\beta_1)-\Phi(\beta_2)+\right. \\ & \alpha_-\left[\alpha_1\Phi(\beta_3)+\alpha_2\Phi(\beta_4)\right]+ \\ & \left.\alpha_+\left[\Phi(\beta_5)-\Phi(\beta_6)\right]\right\}, \end{aligned} \tag{50}$$

where

$$\alpha_\pm = \frac{\exp\left\{\frac{2\Delta}{\tau_F}\left(\Delta\pm\tau_F\kappa\right)\right\}}{1-\exp\left\{\frac{2\Delta^2}{\tau_F}\right\}}, \qquad \alpha_1 = \operatorname{sign}\left(\tau_F-\frac{\Delta}{\kappa}\right), \qquad \alpha_2 = \operatorname{sign}\left(\frac{\Delta}{\kappa}-2\tau_F\right), \tag{51}$$

$$\beta_1 = \sqrt{\frac{\left(\Delta+2\tau_F\kappa\right)^2}{4\tau_F}}, \qquad \beta_2 = \sqrt{\tau_F}\kappa, \qquad \beta_3 = \sqrt{\left(\kappa-\frac{\Delta}{\tau_F}\right)^2\tau_F}, \tag{52}$$

$$\beta_4 = \sqrt{\frac{\left(\Delta-2\tau_F\kappa\right)^2}{4\tau_F}}, \qquad \beta_5 = \left(\Delta+\tau_F\kappa\right)\frac{1}{\sqrt{\tau_F}}, \qquad \beta_6 = \left(\frac{3}{2}\Delta+\tau_F\kappa\right)\frac{1}{\sqrt{\tau_F}}. \tag{53}$$

This result agrees with the asymptotic limit given by Bell [87].

Figure 28 plots the total probability that a fission neutron is thermalized and returned to the nanofuel for a semi-infinite (Eq. 48, black) and finite (Eq. 50, red) Be reflector, using $\tau_F = 97.2$ cm^2 [62] and $L = 18.9$ cm (thermal). This figure shows that the probabilities converge when $\Delta \sim 40$ cm, which implies there is no further reduction in neutron leakage for thicker reflectors.

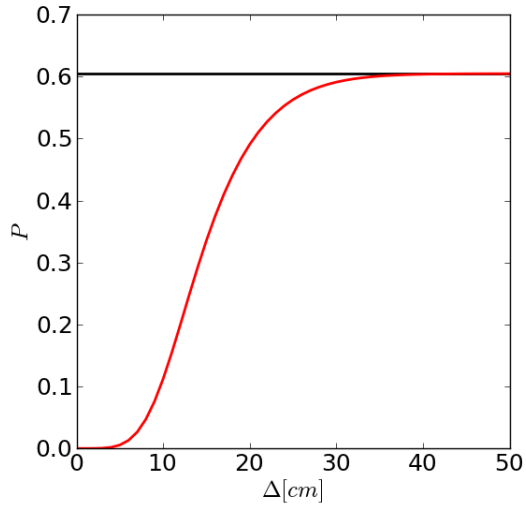


Figure 28: **Total probability that a fission neutron is thermalized and returned to the nanofuel for a semi-infinite (Eq. 48, black) and finite (Eq. 50, red) Be reflector, using $\tau_F = 97.2$ cm^2 [62] and $L = 18.9$ cm.**

B Housing strength

This appendix calculates the reciprocating nanofuel engine piston case (housing) deformation due to an internal gaseous nanofuel pressure using the theory of elasticity, which is described in Landau and Lifshitz [88]. This particular approach is also known as the theory of thick-walled cylinders.

The piston case is a cylinder. Away from the cylinder head and piston, the piston case deformation is entirely in the radial direction. Using cylindrical polar coordinates, the displacement vector ($\mathbf{u}$) is radial and only a function of the radius (R).

In the absence of body forces, the solid body mechanical equilibrium equation is

$$2(1-\sigma)\nabla(\nabla\cdot\mathbf{u}) - (1-2\sigma)\nabla\times(\nabla\times\mathbf{u}) = 0, \tag{54}$$

where σ is the Poisson ratio. Since $u_R = u(R)$, $\nabla\times\mathbf{u} = 0$ and Eq. 54 reduces to

$$\nabla(\nabla\cdot\mathbf{u}) = 0. \tag{55}$$

Following Landau and Lifshitz [88], Eq. 55 has an intermediate solution

$$\nabla\cdot\mathbf{u} = \frac{1}{R}\frac{d(Ru)}{dR} = 2c_1, \tag{56}$$

and a final solution

$$u = c_1 R + \frac{c_2}{R}, \tag{57}$$

where c_1 and c_2 are constants determined by the boundary conditions at the inner and outer surface of the piston case.

The nonzero components of the strain tensor are:

$$u_{RR} = \frac{\partial u_R}{\partial R} = c_1 - \frac{c_2}{R^2}, \tag{58}$$

$$u_{\theta\theta} = \frac{u_R}{R} = c_1 + \frac{c_2}{R^2}. \tag{59}$$

The radial stress tensor is given by

$$\sigma_{RR} = \frac{E}{(1+\sigma)(1-2\sigma)} \left\{ (1-\sigma) u_{RR} + \sigma u_{\theta\theta} \right\}, \tag{60}$$

where E is the Young modulus. Inserting Eqs. 58 and 59 into Eq. 60 gives

$$\sigma_{RR} = \frac{E}{(1+\sigma)(1-2\sigma)} c_1 - \frac{E}{(1+\sigma)} \frac{c_2}{R^2}. \tag{61}$$

The unknown constants c_1 and c_2 are found by assigning the pressure acting on the piston case inner ($\sigma_{RR}(R_{in}) = -p_{in}$) and outer ($\sigma_{RR}(R_{out}) = -p_{out}$) surface. The result is:

$$c_1 = \frac{(1+\sigma)(1-2\sigma)}{E} \frac{p_{in} R_{in}^2 - p_{out} R_{out}^2}{R_{out}^2 - R_{in}^2}, \tag{62}$$

$$c_2 = \frac{(1+\sigma)}{E} \frac{(p_{in} - p_{out}) R_{in}^2 R_{out}^2}{R_{out}^2 - R_{in}^2}. \tag{63}$$

The nonzero components of the stress tensor are:

$$\sigma_{RR} = \frac{p_{in} R_{in}^2 - p_{out} R_{out}^2}{R_{out}^2 - R_{in}^2} - \frac{(p_{in} - p_{out}) R_{in}^2 R_{out}^2}{R_{out}^2 - R_{in}^2} \frac{1}{R^2}, \tag{64}$$

$$\sigma_{\theta\theta} = \frac{p_{in} R_{in}^2 - p_{out} R_{out}^2}{R_{out}^2 - R_{in}^2} + \frac{(p_{in} - p_{out}) R_{in}^2 R_{out}^2}{R_{out}^2 - R_{in}^2} \frac{1}{R^2}, \tag{65}$$

$$\sigma_{zz} = 2\sigma \frac{p_{in} R_{in}^2 - p_{out} R_{out}^2}{R_{out}^2 - R_{in}^2}. \tag{66}$$

In particular, Eq. 65 is known as the hoop stress and has a value at the piston case inner surface of

$$\sigma_{\theta\theta}|_{max} = \frac{p_{in} R_{in}^2 + (p_{in} - 2p_{out}) R_{out}^2}{R_{out}^2 - R_{in}^2}, \tag{67}$$

which is the limiting (most damaging to the structural integrity) stress for the free piston case ($p_{out} \ll p_{in}$). Finally, the radial displacement is given by

$$u = \frac{(1+\sigma)(1-2\sigma)}{E} \frac{p_{in} R_{in}^2 - p_{out} R_{out}^2}{R_{out}^2 - R_{in}^2} R + \frac{(1+\sigma)}{E} \frac{(p_{in} - p_{out}) R_{in}^2 R_{out}^2}{R_{out}^2 - R_{in}^2} \frac{1}{R}. \tag{68}$$

For Be, the temperature dependent yield stress and Young modulus are:

$$\sigma_y[\text{bar}] = 5287.3 - 4.7663T + 0.001T^2, \tag{69}$$

$$E[\text{bar}] = 3.1352 \times 10^6 - 5.6428 \times 10^2 T, \tag{70}$$

respectively, where T is in degrees Kelvin. Be has a melting temperature $T_m = 1,560$ K and a Poisson ratio $\sigma = 0.032$.

References

[1] Thomas S. Kuhn. *The structure of scientific revolutions*. The University of Chicago Press, Chicago, fourth edition, 2012.

[2] Maury Klein. *The power makers: steam, electricity, and the men who invented modern America*. Bloomsbury Press, New York, 2008.

[3] Alvin M. Weinberg. The second nuclear era. *Bulletin of the New York Academy of Medicine*, 59(10):1048–1059, 1983.

[4] Alvin M. Weinberg, Irving Spiewak, Jack N. Barkenbus, Robert S. Livingston, and Doan L. Phung. *The second nuclear era: a new start for nuclear power*. Praeger Publishers, Westport, CT, 1985.

[5] The overnight capital cost refers to the nuclear power plant cost constructed virtually overnight. It includes the engineering, procurement, and construction (EPC) costs associated with the nuclear steam supply system (NSSS), the turbine generator, and the balance of plant (BOP). It also includes the owner's costs associated with site-specific activities, such as: project management, legal services, licensing (state and federal), facilities, taxes, and transmission (local grid improvements). Contingency costs are included; time-dependent costs, such as financing and escalation costs, are excluded.

[6] The all-in capital cost includes the overnight capital cost and time-dependent costs, such as financing and escalation costs.

[7] US Nuclear Regulatory Commission. *NRC: History*. Accessed 23 April 2015. `http://www.nrc.gov/about-nrc/emerg-preparedness/history.html`.

[8] Jonathan Koomey and Nathan E. Hultman. A reactor-level analysis of busbar costs for US nuclear plants, 1970-2005. *Energy Policy*, 35:5630–5642, 2007.

[9] US Nuclear Regulatory Commission Regulations: Title 10, *Code of Federal Regulations*, §50.

[10] US Department of Energy. US Energy Information Administration. Office of Energy Analysis. *International energy outlook 2013: with projections to 2040*. DOE/EIA-0484(2013), July 2013.

[11] OECD member countries include: Australia, Austria, Belgium, Canada, Chile, Czech Republic, Denmark, Estonia, Finland, France, Germany, Greece, Hungary, Iceland, Ireland, Israel, Italy, Japan, Luxembourg, Mexico, Netherlands, New Zealand, Norway, Poland, Portugal, Slovakia, Slovenia, South Korea, Spain, Sweden, Switzerland, Turkey, United Kingdom, and United States.

[12] US Environmental Protection Agency. *Climate change indicators in the United States: atmospheric concentration of greenhouse gases*. August 2013.

[13] Susan Solomon, Dahe Qin, Martin Manning, Melinda Marquis, Kristen Averyt, Melinda M. B. Tignor, Henry LeRoy Miller, and Zhenlin Chen. *Climate change 2007: the physical science basis*. Cambridge University Press, New York, 2007.

[14] Anthony D. Barnosky, Elizabeth A. Hadly, Jordi Bascompte, Eric L. Berlow, James H. Brown, Mikael Fortelius, Wayne M. Getz, John Harte, Alan Hastings, Pablo A. Marquet, Neo D. Martinez, Arne Mooers, Peter Roopnarine, Geerat Vermeij, John W. Williams, Rosemary Gillespie, Justin Kitzes, Charles Marshall, Nicholas Matzke, David P. Mindell, Eloy Revilla, and Adam B. Smith. Approaching a state shift in Earth's biosphere. *Nature*, 486:52–58, 2012.

[15] Gal Luft and Anne Korin. *Energy security challenges for the 21st century: a reference handbook*. Praeger Publisher, Westport, CT, 2009.

[16] James J. Duderstadt and Louis J. Hamilton. *Nuclear reactor analysis*. John Wiley & Sons, New York, 1976.

[17] Charles Fayette Taylor. *The internal-combustion engine in theory and practice; volume I: thermodynamics, fluid flow, performance*. The MIT Press, Cambridge, second revised edition, 1985.

[18] US Nuclear Regulatory Commission Regulations: Title 10, *Code of Federal Regulations*, §52.

[19] Jay M. Gutierrez and Alex S. Polonsky. *Fundamentals of nuclear regulation in the United States*. Morgan Lewis, Second edition, July 2007.

[20] Robert Rosner and Stephen Goldberg. Analysis of GW-scale overnight capital costs. Technical report, University of Chicago, EPIC, November 2011.

[21] J. Hempstead, D. Aschenbach, A. J. Sabatelle, M. Haggarty, L. Schumacher, and W. L.

Hess. New nuclear generation: ratings pressure increasing. Technical report, Moody's Investors Service, June 2009.

[22] William D. Magwood. Report to congress on small modular nuclear reactors. Technical report, US Department of Energy, May 2001.

[23] D. T. Ingersoll. Deliberately small reactors and the second nuclear era. *Progress in Nuclear Energy*, 51:589–603, 2009.

[24] T. P. Wright. Factors affecting the cost of airplanes. *Journal of Aeronautical Science*, 4(4):122–128, 1936.

[25] Robert Rosner, Stephen Goldberg, and Joseph S. Hezir. Small modular reactors — key to future nuclear power generation in the U.S. Technical report, University of Chicago, EPIC, November 2011.

[26] R. W. Bussard and Richard D. DeLauer. *Nuclear rocket propulsion.* McGraw-Hill, New York, 1958.

[27] Edward H. Kerner. The expansion of a fissionable gas as a source of atomic power. *Journal of Applied Physics*, 24:815–6, 1953.

[28] Richard L. Moore. Nuclear reactor motor. US Patent: 3,549,490, issue date 22 Dec 1970.

[29] Joseph A. Pettibone. A novel scheme for making cheap electricity with nuclear energy. Technical Report UCID-18153, LLNL, August 1979.

[30] Joseph S. Pettibone. A novel scheme for making cheap electricity with nuclear energy. Technical Report UCRL-JC-107068, LLNL, April 1991.

[31] Karlheinz Thom. Review of fission engine concepts. *Journal of Spacecraft and Rockets*, 9(9):633–639, 1972.

[32] K. Thom and R. T. Schneider. Fissioning uranium plasmas. *Nuclear data in science and technology*, 1:15–38, 1975.

[33] Peter Alesso, Tze-Show Chow, Ralph Condit, John Heidrich, Joseph Pettibone, and Ronald Streit. Inherently safe nuclear-driven internal combustion engines. Technical Report UCRL-JC-107417, LLNL, June 1991.

[34] John Heidrich, Joseph Pettibone, Tze-Show Chow, Ralph Condit, and George Zimmerman. Gaseous core nuclear-driven engines featuring a self-shutoff mechanism to provide nuclear safety. Technical Report UCRL-JC-108959, LLNL, November 1991.

[35] John Heidrich, T. Scott Carman, Tze-Show Chow, Ralph Condit, B. Grant Logan, and Joseph Pettibone. Nuclear-driven technologies that could reduce the cost of electricity by several fold. Technical Report UCRL-JC-108960, LLNL, November 1991.

[36] Neil E. Todreas and Mujid S. Kazimi. *Nuclear systems: volume 1: thermal hydraulic fundamentals*. CRC Press, New York, second edition, 2012.

[37] John B. Heywood. *Internal combustion engine fundamentals*. McGraw-Hill, New York, 1988.

[38] Samuel Glasstone and Milton C. Edlund. The elements of nuclear reactor theory. Part I. Technical Report 1099, ORNL, 1952.

[39] Robert V. Meghreblian and David K. Holmes. *Reactor analysis*. McGraw-Hill Book Company, New York, 1960.

[40] Weston M. Stacey. *Nuclear reactor physics*. Wiley-VHC Verlag GmbH & Co., Germany, second edition, 2007.

[41] Richard P. Feynman. There's plenty of room at the bottom. *Engineering and science*, 23:22, 1960.

[42] Atomic Energy Act of 1954, as Amended. Public Law 83-703 (30 August 1954).

[43] M. C. Regalbuto. Alternative separation and extraction: UREX+ processes for actinide and targeted fission product recovery. In Kenneth L. Nash and Gregg J. Lumetta, editors, *Advanced separation techniques for nuclear fuel reprocessing and radioactive waste treatment*. Woodhead Publishing, Philadelphia, 2011.

[44] E. R. Jette, J. F. Lemons, and A. E. Florin. Plutonium hexafluoride: second report on the preparation and properties. Technical Report LA-1168, LANL, November 1950.

[45] Bernard Weinstock and John G. Malm. The properties of plutonium hexafluoride. *Journal of inorganic and nuclear chemistry*, 2:380–394, 1956.

[46] Martin J. Steindler. Laboratory investigations in support of fluid bed fluoride volatility processes: part II, the properties of plutonium hexafluoride. Technical Report ANL-6753, ANL, August 1963.

[47] X-5 Monte Carlo Team. MCNP — a general Monte Carlo N-Particle transport code, version 5. Technical Report LA-UR-03-1987, LANL, February 2008.

[48] Forrest B. Brown. The makxsf code with Doppler broadening. Technical Report LA-UR-06-7002, LANL, 2006.

[49] John R. Lamarsh. *Introduction to nuclear engineering*. Addison-Wesley Publishing Company, Reading, Massachusetts, second edition, 1983.

[50] David L. Hetrick. *Dynamics of nuclear reactors*. American Nuclear Society, La Grange Park, Illinois, 1993.

[51] All-Russia Research Institute of Automatics. *VNIIA - neutron generators*. Accessed 20 March 2015. `http://www.vniia.ru/eng/ng/index.html/`.

[52] Activation Technology Corporation. *N550*. `http://www.atcng.com/n550.htm/`.

[53] J. W. Mather. Investigation of the high-energy acceleration mode in the coaxial gun. *Physics of Fluids*, 7(11):S28–S34, 1964.

[54] J. W. Mather. Formation of a high-density deuterium plasma focus. *Physics of Fluids*, 8(2):366–377, 1965.

[55] J. W. Mather. Dense plasma focus. In *Methods of Experimental Physics*, volume 9B, pages 187–249. Elsevier, 1971.

[56] L. Michel, K. H. Schonbach, and Heinz Fischer. Neutron emission from a small 1-kJ plasma focus. *Applied Physics Letters*, 24(2):57–59, 1974.

[57] G. Decker, W. Kies, and G. Pross. The first and the final fifty nanoseconds of a fast focus discharge. *Physics of Fluids*, 26(2):571–578, 1983.

[58] G. Decker, W. Kies, M. Malzig, C. van Calker, and G. Ziethen. High performance 300 kV driver SPEED 2 for MA pinch discharges. *Nuclear Instruments and Methods in Physics Research A*, 249:477–483, 1986.

[59] William D. Schulz. Two-Dimensional Lagrangian Hydrodynamic Difference Equations. Technical Report UCRL-6776, LRL, April 1963.

[60] Robert D. Richtmyer and K. W. Morton. *Difference methods for initial-value problems*. Interscience Publishers, New York, second edition, 1967.

[61] William H. Press, Saul A. Teukolsky, William T. Vetterling, and Brian P. Flannery. *Numerical recipes in fortran: the art of scientific computing*. Cambridge University Press, New York, second edition, 1992.

[62] R. J. Templin. Reactor physics constants. Technical Report 5800, ANL, July 1963.

[63] R. M. Ferrer, S. Bays, and M. Pope. Evaluation of homogeneous options: effects of minor actinide exclusion from single and double tier recycle in sodium fast reactors. Technical Report INL/EXT-08-14034, INL, March 2008.

[64] S. Bays, H. Zhang, and M. Pope. Deep burn fuel cycle integration: evaluation of two-tier scenarios. Technical Report INL/EXT-09-15915, INL, May 2009.

[65] Charles G. Bathke, Bartley B. Ebbinghaus, Brad W. Sleaford, Richard K. Wallace, Brian A. Collins, Kevin R. Hase, Gordon D. Jarvinen, Keith S. Bradley, John R. Ireland, M. W. Johnson, Andrew W. Prichard, and Brian W. Smith. The attractiveness of materials in advanced nuclear fuel cycles for various proliferation and theft scenarios. Technical Report LA-UR-09-02466, LANL, 2009.

[66] Kenichi Yamamoto. *Rotary engine*. Toyo Kogyo Co., Hiroshima, Japan, 1971.

[67] Kenichi Yamamoto. *Rotary engine*. Sankaido Co., Tokyo, Japan, 1981.

[68] Kenneth C. Weston. *Energy conversion*. PWS Publishing Company, Boston, 1992.

[69] David H. Nash. Rotary engine geometry. *Mathematics Magazine*, 50(2):87–89, March 1977.

[70] US Nuclear Regulatory Commission Regulations: Title 10, *Code of Federal Regulations*, §50.2.

[71] US Nuclear Regulatory Commission. Policy statement on the regulation of advanced reactors. *Federal Register*, 73(199):60612, October 2008.

[72] E. Teller, M. Ishikawa, L. Wood, R. Hyde, and J. Nuckolls. Complete automated nuclear power reactors for long-term operation: III. enabling technology for large-scale, low-risk affordable nuclear electricity. Technical Report UCRL-JRNL-122708, LLNL, 2003.

[73] US Department of Energy. US Energy Information Administration. Office of Energy Analysis. *Updated capital cost estimates for electricity generation plants*. November 2010.

[74] US Department of Energy. US Energy Information Administration. Independent Statistics & Analysis. *Updated capital cost estimates for utility scale electricity generation plants*. April 2013.

[75] S. Inwood. Program on technology innovation: integrated generation technology options. Technical Report 1022782, EPRI, June 2011.

[76] US Department of Energy. Office of Nuclear Energy, Science and Technology. *A roadmap to deploy new nuclear power plants in the United States by 2010: volume I summary report*. October 2001.

[77] US Department of Energy. Office of Nuclear Energy, Science and Technology. *A roadmap*

to deploy new nuclear power plants in the United States by 2010: volume II main report. October 2001.

[78] US Department of Energy. *Report on lessons learned from the NP 2010 early site permit program: final report*. Prepared by Energetics Incorporated. 26 March 2008.

[79] US Department of Energy. US Energy Information Administration. Independent Statistics & Analysis. *Electric power annual 2012*. December 2013.

[80] US Department of Energy. US Energy Information Administration. Independent Statistics & Analysis. *Henry Hub natural gas spot price (dollars per million Btu)*. Accessed 6 May 2015. `http://www.eia.gov/dnav/ng/hist/rngwhhdm.htm/`.

[81] US Department of Energy. US Energy Information Administration. Independent Statistics & Analysis. *Coal — U.S. Energy Information Administration (EIA)*. Accessed 6 May 2015. `http://www.eia.gov/coal/`.

[82] US Department of Energy. Blue Ribbon Commission on America's Nuclear Future. *Blue ribbon commission on America's nuclear future: report to the Secretary of Energy*. January 2012.

[83] New York State Energy Research and Development Authority. *Western New York Nuclear Service Center background and history*. By Paul J. Bembia. 27 April 2011.

[84] Thomas C. Reed and Danny B. Stillman. *The nuclear express: a political history of the bomb and its proliferation*. Zenith Press, Minneapolis, MN, 2009.

[85] Anthony Andrews. *Nuclear fuel reprocessing: U.S. policy development*. Congressional Research Service Report for Congress, March 2008.

[86] Water.org. *Water facts: water*. Accessed 17 February 2015. `http://water.org/water-crisis/water-facts/water/`.

[87] George I. Bell. Calculations of the critical mass of UF_6 as a gaseous core, with reflectors of D_2O, Be and C. Technical Report LA-1874, LANL, February 1955.

[88] L. D. Landau and E. M. Lifshitz. *Theory of elasticity (course of theoretical physics; volume 7)*. Pergamon Press, Boston, third edition, 1986.